Electronic Structure of Three-Coordinate Fe^{II} and Co^{II} β-Diketiminate Complexes

Alexandra L. Nagelski,[†] Mykhaylo Ozerov,[#] Majed S. Fataftah,[†] J. Krzystek,[#] Samuel M. Greer,[$] Patrick L. Holland,[†]* and Joshua Telser[§]*

[†] Department of Chemistry, Yale University, New Haven, Connecticut 06511, United States

[#] National High Magnetic Field Laboratory, Florida State University, Tallahassee, Florida 32310, United States

[$] Los Alamos National Laboratory, Los Alamos, New Mexico 87545, United States

[§] Department of Biological, Chemical and Physical Sciences, Roosevelt University, Chicago, Illinois 60605, United States

Corresponding authors email:
patrick.holland@yale.edu (P. L. H.), jtelser@roosevelt.edu (J. T.)

Abstract

The β-diketiminate supporting group, $[ArNCRCHCRNAr]^-$, stabilizes low coordination number complexes. Four such complexes, where R = *tert*-butyl, Ar = 2,6-diisopropylphenyl, are studied: (nacnac^{rBu})ML, where M = Fe^{II}, Co^{II} and L = Cl, CH_3. These are denoted **FeCl**, **FeCH$_3$**, **CoCl**, and **CoCH$_3$** and have been previously reported and structurally characterized. The two Fe^{II} complexes (S = 2) have also been previously characterized by Mössbauer spectroscopy, but only indirect assessment of the ligand-field splitting and zero-field splitting (zfs) parameters was available. Here, EPR spectroscopy is used, both conventional field-domain for the Co^{II} complexes (with S = 3/2) and frequency-domain, far-infrared magnetic resonance spectroscopy (FIRMS) for all four complexes. The Co^{II} complexes were also studied by magnetometry. These studies allow accurate determination of the zfs parameters. The two Fe^{II} complexes are similar with nearly axial zfs and large magnitude zfs given by $D = -37 \pm 1$ cm^{-1} for both. The two Co^{II} complexes likewise exhibit large and nearly axial zfs, but surprisingly **CoCl** has positive D = +55 cm^{-1} while **CoCH$_3$** has negative D = –49 cm^{-1}. Theoretical methods were used to probe the electronic structures of the four complexes, which explain the experimental spectra and the zfs parameters.

Introduction

First row transition metal (3d) complexes with low-coordination numbers, defined here as two- or three-coordinate, have generated considerable interest in the inorganic chemistry community.[1-13] In particular, the area of single molecule magnets (SMMs)[14-17] has been greatly advanced by investigations of low-coordinate 3d ion complexes.[18-39] The properties of SMMs depend crucially on the details of the ligand-field splitting of the orbitals and the zero-field splitting (zfs) of the magnetic sublevels,[40-42] adding strong motivation to quantitatively determine these parameters.

One N-donor ligand that has been particularly effective at stabilizing three-coordinate complexes is the β-diketiminate ion,[43-46] often denoted nacnac, due to its formal derivation from β-diketonate, or acac.[47] An advantage of nacnac over acac is the ability to incorporate steric bulk on the imine/iminate substituents,[45] to prevent formation of four- and six-coordinate transition metal complexes that are common with β-diketonates,[48] e.g., $(acac)_2M$, M = Cu, Pd; $(acac)_3M$, M = Ti, V, Cr, Mn, Fe, Co, etc.; the CSD (version 5.43, update 4) yields 355 structures of 4-coordinate bis(acac) complexes (of which 245 are M = Cu) and 378 structures of 6-coordinate tris(acac) complexes. In contrast, there are only two structurally characterized complexes of $(nacnac^{R,R'})_3M$; with $M = Cr^{III}$ (CSD: IJEVUP, IJEWAW)[49] and with Y^{III} (CSD: XINMAJ).[50] In the former, the *N*-substituents are benzyl ($nacnac^{Bn,Me}$) and in the latter phenyl ($nacnac^{Ph,Me}$). Four-coordinate bis(nacnac) complexes are relatively plentiful, with 108 structures, although this includes tetraazamacrocylic complexes such as these of Ni^{II}.[51] There are 48 structures of $(nacac^{R,Me})_2M$ transition metal complexes with two bidentate ligands. With bulky *N*-substituents, most commonly 2,6-diisopropylphenyl (DiPP) groups, the three-coordinate complexes of general formula $(nacnac^{R,R'})MX$ are often isolable, with the CSD yielding 401 structures wherein M = Fe, Co, Ni, Cu, Zn (primarily), and X = C, N, P, O, S, halide, etc. Specifically with the DiPP substituent, there are 255 structures of $(nacnac^{DiPP,R'})MX$. Thus, this is a useful scaffold for constructing systematic series of three-coordinate complexes.

Our focus here is on two 3d ions of great importance in inorganic chemistry in general, and in the area of SMMs in particular, namely Fe^{II} and Co^{II}. These ions feature rich d-orbital manifolds when they have high-spin d^6 and d^7 electronic configurations, respectively. Cobalt(II) complexes are among the most extensively studied in connection with SMM behavior, as has been very recently reviewed,[52] but SMM examples of Fe^{II}, particularly in low-coordination number, are also plentiful such as in these recent

examples.[31, 33, 34, 36] For the detailed study here, we utilize two ligands in the third coordination position, X = Cl and CH_3. These represent respectively a moderate σ- and π-donor and a strong σ-donor. Both have cylindrical symmetry (i.e., when *z* is chosen as the M-X σ-bond vector, the *x* and *y* directions are equivalent). These four complexes, which have been previously reported by some of us,[4, 53, 54] are testbeds for investigating the electronic structure of 3-coordinate complexes of high-spin 3d ions. In these complexes, an extremely bulky β-diketiminate ligand is used, 2,2,6,6-tetramethyl-3,5-bis(2,6-diisopropylphenylimido)heptane anion, nacnac^{DiPP,tBu}, which we will abbreviate as nacnac^{tBu}. For further simplicity, the four (nacnac^{DiPP,tBu})MX (M= Fe, Co; X = Cl, CH_3) complexes will be referred to respectively as **FeCl**, **FeCH$_3$**, **CoCl**, and **CoCH$_3$** and collectively as **MX** and pairwise by metal as **FeX** or **CoX** and by ligand as **MCl** or **MCH$_3$**.

Using applied-field Mössbauer effect spectroscopy, certain aspects of the electronic structure of the **FeX** complexes have been investigated previously;[4] however, the computational tools available at that time were insufficient for a deeper study by quantum chemical theory. Mössbauer gives an indirect assessment of the ligand-field transitions of the iron complexes, and is of course inapplicable to the cobalt complexes. Here, we use a more direct measurement of ligand-field parameters, far-infrared magnetic resonance spectroscopy (FIRMS)[55, 56]. FIRMS directly yields the zfs of high-spin systems, which is key towards understanding their electronic structure. The results obtained herein give insights that may be applicable to other high-spin ions and to other complexes of the versatile and popular β-diketiminate ligand platform.

Experimental Section

Synthesis. The complexes **FeCl**, **FeCH$_3$**, **CoCl**, and **CoCH$_3$** were prepared as previously reported.[4, 54, 57] All sample handling was done under an inert atmosphere.

Electronic absorption spectroscopy. Electronic absorption spectra of all complexes were recorded in toluene solution on a Cary 60 spectrophotometer.

Caution! Care should be taken in the presence of high magnetic fields and in the use of cryogenic fluids.

X- and Q-Band EPR/ENDOR spectroscopy. X-band (~9.5 GHz) spectra of **CoCl** and **CoCH$_3$** in toluene frozen solution and as pure powders were recorded on a modified Bruker E109 spectrometer equipped with an Oxford cryostat. Q-band (35 GHz) EPR and ENDOR spectra only of frozen solution samples were recorded at 2 K on CW[58] and pulsed[59]

spectrometers previously described, the latter using the Davies pulse sequence[60] for ^{14}N ENDOR. CW EPR spectra under these conditions are in rapid passage and thus exhibit an absorption lineshape.[61, 62] EPR simulations used the program QPOW[63, 64] and ENDOR simulations used the locally written program DDPOWHE.

Magnetometry. Magnetic measurements for **CoX** were performed using a Quantum Design MPMS 3 magnetometer. All samples were prepared under a N_2 atmosphere in polyethylene capsules and were solid powders restrained with eicosane in a gelatin capsule. Ferromagnetic impurities were ruled out by inspection of the 100 K magnetization data that showed no curvature in the field range of 0 – 7 T. DC magnetic susceptibility measurements were collected in the temperature range of 2 – 300 K under an applied magnetic field of 0.1 T. Variable-temperature, variable-field (VTVH) magnetization measurements were collected in the temperature range of 2–10 K under applied magnetic fields of 1 – 7 T, in 1 T increments. DC magnetic susceptibility measurements were corrected for diamagnetism, estimated using Pascals constants.[65] Magnetic susceptibility and VTVH magnetization data were simulated using the program MagProp in DAVE 2.0.[66]

FIRMS. FIRMS experiments were performed at NHMFL using a Bruker Vertex 80v FT-IR spectrometer coupled with a 17 T vertical-bore superconducting magnet in a Voigt configuration (light propagation perpendicular to the external magnetic field). The experimental setup employs broadband terahertz radiation emitted by an Hg arc lamp. The radiation transmitted through the sample is detected by a composite silicon bolometer (Infrared Laboratories) mounted at the end of the quasi-optical transmission line. Both the sample and bolometer are cooled by low-pressure helium gas to a temperature of 5.5 K. To obtain air-free measurements, the samples were loaded in the sample holder in an argon-filled glovebox. The microcrystalline powder (~3 – 5 mg) was bonded by *n*-eicosane and sandwiched between two *n*-eicosane layers for protection from oxygen and moisture. Sample loading in the FIRMS spectrometer was performed under a flow of N_2. After collection, the samples were exposed to ambient conditions for two days, after which the measurements were recollected to ensure the originally observed absorption peaks were not attributable to sample degradation from contact with oxygen or moisture (Figures S8 and S9). The intensity spectra of each sample were measured in the spectral region between 14 and 730 cm^{-1} (0.42 − 22 THz) with a resolution of 0.3 cm^{-1} (9 GHz). To discern the magnetic absorptions, the spectra were normalized by dividing with the reference spectrum, which is the average spectrum for all magnetic fields. Such

normalized transmittance spectra are sensitive only to intensity changes induced by the magnetic field and therefore are not obscured by nonmagnetic vibrational absorption features. The data analysis was implemented using an in-house written MATLAB code and the EPR simulation software package EasySpin,[67, 68] which uses a standard spin Hamiltonian for $S = 2$ (**FeX**) and $S = 3/2$ (**CoX**).[69]

Ligand Field Theory (LFT) Calculations. Calculations employed the locally written programs DDN and DDNFIT and the Ligfield software by Bendix (Copenhagen U., Denmark).[70] These programs employ all 210 microstates for d^6 (**FeCl**, **FeCH$_3$**), and all 120 microstates for d^7 (**CoCl**, **CoCH$_3$**) with the angular overlap model (AOM)[71-73] to describe σ- and π-bonding using respectively the parameters ε_σ and ε_π (which can be anisotropic: $\varepsilon_{\pi-s}$ and $\varepsilon_{\pi-c}$).

Quantum Chemical Theory (QCT) Calculations. All calculations were performed using the Orca 4.2 program package.[74] Density Functional Theory (DFT) was used to calculate the ^{57}Fe quadrupole splitting (ΔE_Q) and isomer shift (δ) for **FeX**, and the ^{57}Fe and ^{59}Co **A**-tensors and for **CoX** the ^{14}N **A**- and **P**-tensors. Calculations were performed using the atomic coordinates from the reported X-ray structures using the B3LYP/ CP(PPP) (Fe, Co), def2-TZVP (N, Cl, coordinated C), def2-SVP (C/H) functional/basis set combination.[75-78] The calculated electron density at the Fe nuclei were converted into ^{57}Fe Mössbauer isomer shift values using the calibration reported by Römelt et. al. [79] For these calculations the spin-orbit coupling operator was computed using the mean-field approximation (SOMF). Time Dependent DFT (TD-DFT) calculations were performed with the same functional/basis set described above except for Fe/Co which were changed to def2-tzvp. The TD-DFT calculations included 250 roots and the computed UV-visible absorption spectrum is reported in the SI.

The state averaged-CASSCF (SA-CASSCF) calculations used the minimum active space of six (**FeX**) or seven (**CoX**) electrons in the five 3d orbitals and, for **FeX**, included all five quintet and all 45 triplet states while the **CoX** compounds considered all 10 quartet and all 40 doublet states.

The resolution of the identity approximation and auxiliary basis sets generated using the 'autoaux' command were used in all CASSCF calculations.[80] Scalar relativistic effects were accounted for by the second-order Douglas-Kroll-Hess (DKH) procedure and appropriate basis sets dkh-def2-TZVP (Fe, N, Cl, coordinated C) and dkh- def2-SVP (C/H).[81] The converged wavefunctions were then subjected to N-electron valence

perturbation theory to second order (NEVPT2) to account for dynamic correlation.[82] Example ORCA input files are shown in the Supporting Information.

Results and Discussion

Structures. The crystal structures of all four complexes have been reported previously: **FeCl**,[53] (CSD: REWZUO), **FeCH$_3$**,[4] (CSD: XOXHUN), and **CoCl** (CSD: XUNTAB) and **CoCH$_3$** (CSD: XUNTEF).[54] All four complexes have a crystallographic two-fold symmetry axis coincident with the X-M vector so that the two ∠N-M-X (X = Cl, C) are equal and the molecules have roughly C_{2v} point group symmetry. This C_2 axis would normally be defined as the *z* axis, but given that these complexes are derived from trigonal planar geometry, we define the *z* axis as the pseudo three-fold axis (i.e., normal to the molecular plane) and the actual C_2 axis is defined as *x*. This assignment, which was used also by Andres et al. for the Fe^{II} complexes,[4] leads to a slight redefinition of the d orbital representations in C_{2v} symmetry as described elsewhere and is shown in Table S7.[83] Andres et al. also presented a d orbital energy scheme for both the "parent" trigonal planar (i.e., a hypothetical MX$_3$ complex with D_{3h} (or C_{3h}) symmetry[84]) and the actual structure. As such a diagram is extremely useful for both the Fe^{II} and Co^{II} complexes under study here, we reproduce it with slight modifications. Note that if there were only σ-bonding, then the degenerate d_{xz}, d_{yz} orbitals would be lowest in energy; however, π-donation from the N donors (and from Cl in **MCl**) raises d_{xz}, d_{yz} above d_{z^2}; the σ-antibonding degenerate $d_{xy}, d_{x^2-y^2}$ orbitals are always highest in energy. Quantitative diagrams are given in Figures 10 and 11 for **FeX** and **CoX**, respectively. The hypothetical trigonal Co^{II} complex is Jahn-Teller effect (JTE) active (^{4}E″ ground state), so it would distort as in actual trigonal complexes, such as Mo^{III}.[85] However, there is no threefold symmetry in the present Fe^{II} and Co^{II} complexes, because the bidentate β-diketiminate ligand constrains ∠N-M-N to roughly 95°. As a result, none of the (nacnac)MX complexes has an orbitally degenerate JTE active ground state; the ground state for **FeX** (X = Cl, CH$_3$) is ^{5}A$_1$ and for **CoX** is ^{4}A$_2$.

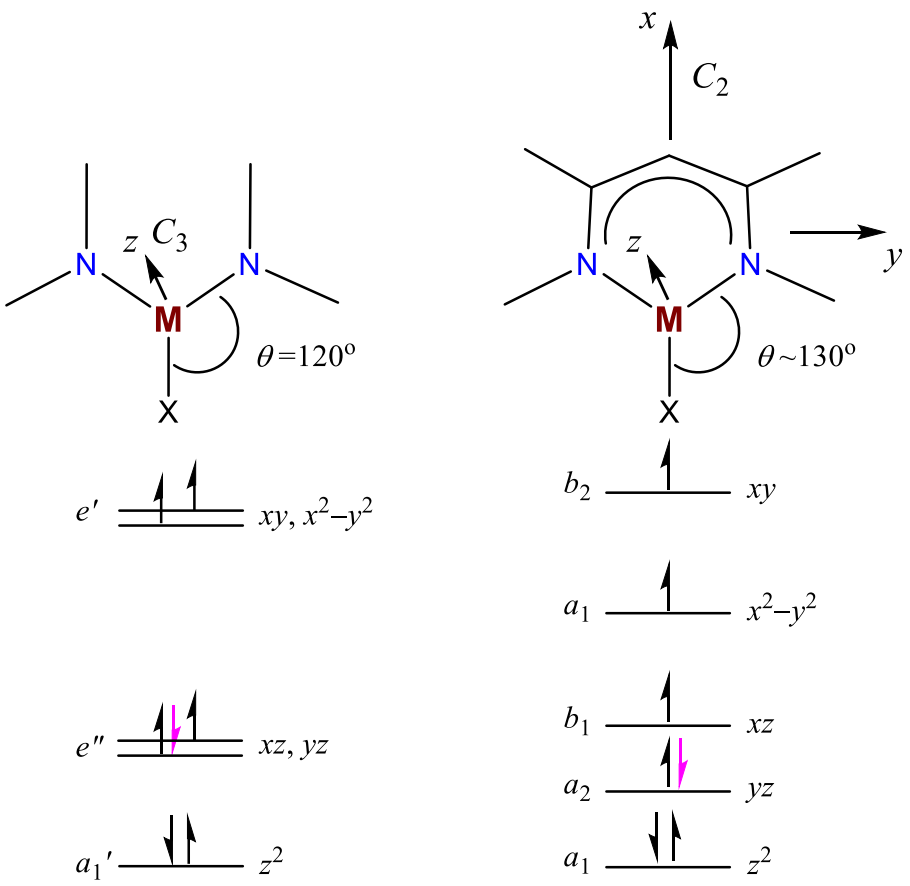

Figure 1. Qualitative d orbital energy diagram for (nacnac)MX complexes. The left diagram is for an idealized trigonal planar geometry (i.e., θ = 120°) with labels for D_{3h} symmetry (thus ignoring the difference between N and X ligands). In the case of only σ-bonding, the $d_{xz,yz}$ orbitals would be lowest in energy; out-of-plane π-bonding (donation) by the N and X ligands raises them above d_{z^2} in energy. The right diagram is for the idealized real geometry: planar but no longer trigonal (i.e., $\theta \approx 130°$). The labels are for C_{2v} symmetry, but with the z axis of the Cartesian coordinate frame out of plane and the x axis along the C_2 axis to correspond to the D_{3h} definition. This leads to d_{yz} having a_2 representation and d_{xy} having b_2 representation, the reverse of the standard C_{2v} definition. Orbital occupancy is shown with black arrows for Fe^{II} (d^6, S = 2) and the magenta arrow additionally for Co^{II} (d^7, S = 3/2). Adapted from Figure 10 in Andres et al.[4] Copyright 2002 American Chemical Society.

Conventional (field-domain) EPR spectroscopy. X-band EPR spectra using parallel mode detection[86-90] were reported by Andres et al. for powder **FeCl** and **FeCH$_3$**.[4] The two Fe^{II} complexes each exhibited an X-band (9.27 GHz) signal at low field (maxima at 35.6 mT and 59.4 mT for **FeCl** and **FeCH$_3$**, respectively; see Figure 8 in Andres et al.[4]). This high g' value (~18.6 and ~11.2, respectively) signal arises from a transition within the $m_S = \pm 2$ quasi-doublet,[86, 88, 91] which is the spin ground state (i.e., $D < 0$) as indicated by its temperature dependence. The energy levels for both $S = 3/2$ and $S = 2$ systems are shown in Figure 2.

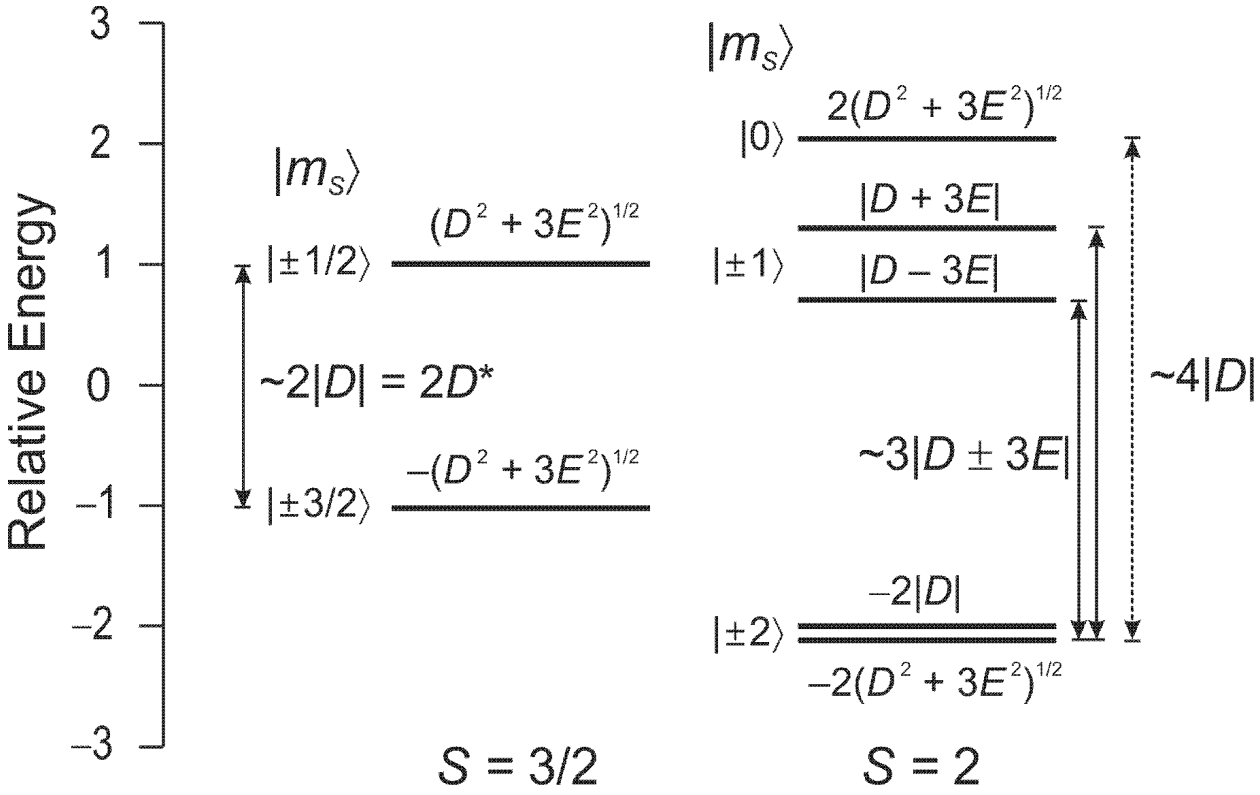

Figure 2. Energy levels for spin sublevel states in quartet (left) and quintet (right) systems with $D < 0$. For illustrative purposes, the rhombicity is small ($|E/D| = 0.1$ for both). An EPR transition within the small splitting (~$0.03|D|$) between the $m_S = \pm 2$ levels is observed at X-band for **FeCl** and **FeCH$_3$**.[4] The transitions indicated by arrows can be observed by FIRMS (both transitions to the $m_S = \pm 1$ levels for $S = 2$ are readily observable while that to the $m_S = 0$ level is less likely and is thus shown as a dotted line).

The X-band spectrum of **CoCl** in toluene solution is shown in Figure 3; the Supporting Information shows the X-band spectrum of powder **CoCl** (Figure S3) as well

as the corresponding Q-band spectra (CW and pulsed; Figure S4). The Q-band toluene frozen solution spectrum is essentially the same as at X-band except for the loss of hyperfine resolution due to *g*-strain,[92] but with slightly better determination of *g* values. The X-band spectra for the solid and frozen solution are essentially the same, except for the inevitable loss of resolution in the magnetically non-dilute powder, which indicates that the solid state (XRD) structure is maintained in toluene solution. Qualitatively, the conventional EPR spectra of **CoCl** are characteristic of an $S = 3/2$ system with zfs ($2D^*$, $D^* = (D^2 + 3E^2)^{1/2}$) that is large in energy relative to the microwave quantum (~1.17 cm^{-1} at Q-band) and with $D > 0$, i.e., $m_S = \pm 1/2$ ground state.[91, 93, 94] The simulations thus employ an effective spin, $S' = 1/2$, with effective g' values, as opposed to the real $S = 3/2$. Use of perturbation theory formulas[91, 95] allows an estimate as to the real *g* values along with the zfs rhombicity, $|E/D|$. These formulas give $|E/D| = 0.065$ and $g_x = 2.580$, $g_y = 2.585$, $g_z = 2.000$ ($g_{iso} = 2.39$), which parameter set affords **g′** = [4.644, 5.655, 1.975], coinciding with the experimental **g′** = [4.62 – 4.70, 5.64 – 5.68, 1.96 – 1.97] (here ordered as g'_x, g'_y, g'_z, rather than as g'_{max}, g'_{mid}, g'_{min}, as in the simulation) with the range due to the use of two frequencies and different sample preparations. The real **g** tensor is thus essentially axial with $g_\perp > 2$, $g_\parallel \approx 2$, and $2 < g_{iso} < 2.5$, which is typical for d^7 systems.

The ^{59}Co hyperfine coupling is very well resolved at $g'_\parallel$ with an average splitting of 8.4 mT. The ^{59}Co hyperfine coupling tensor determined by simulation is also an effective one, **A′**(^{59}Co), i.e., defined in terms of coupling to $S' = 1/2$, rather than to $S = 3/2$.[96] It can be converted to a real (i.e., intrinsic) **A**(^{59}Co) by multiplying each component by g_i/g'_i,[97] so that **A**(^{59}Co) ≈ [220, 320, 210] MHz (here ordered as A_x, A_y, A_z, as with **g**), which gives $A_{iso} \approx 250$ MHz. EPR spectra of high-spin Co^{II} typically exhibit broad linewidths so that ^{59}Co hyperfine coupling is unresolved.[98] This is presumably a function of *g*- and *A*-strain (i.e., a distribution in these parameters due to structural heterogeneity) as well as superimposed ligand hyperfine coupling (typically from ^{14}N, but also ^{31}P[98]). One example where $A(^{59}Co)$ was well resolved is a five-coordinate complex with only O-donors ($I = 0$ ligands), pentakis(2-picoline *N*-oxide)cobalt(II) perchlorate, prepared as a doped powder (< 0.1 mol%) in the isomorphous Zn^{II} host.[98] This system exhibits **g′** = [5.96, 3.56, 1.91] – thus similar values to **CoCl**, and hyperfine structure was resolved in both the g_{max} and g_{min} (g_z, $g_\parallel$) regions corresponding to an average $A(^{59}Co) = 243$ MHz, essentially the same A_{iso} value as seen here. An EPR study by Tierney and co-workers of dihydrido[diphenyl]bis([3,4,5-methyl]-1-pyrazolyl)borate ([Ph_2]Bp^{nMe}) complexes of Co^{II} presented species with both $m_S = \pm 1/2$ and $m_S = \pm 3/2$ signals with resolved $A(^{59}Co)$ on

certain features,[99] despite the ^{14}N-donor ligands. For example, $(Ph_2Bp)_2Co$ had **g′** = [5.50, 4.59, 2.00] – very close to **CoCl**, while Bp_2Co had **g′** = [4.73, 4.67, 2.03] – far more axially symmetric than **CoCl**, but with $A(^{59}Co)_z$ = 298 MHz,[99;100] still similar to that for **CoCl**. The hyperfine coupling for **CoCl** is also near those measured for low-spin Co^{II} macrocyclic complexes with N4 coordination.[101] Quantitative analysis of the spin Hamiltonian parameters for **CoCl** is given below in the computational section.

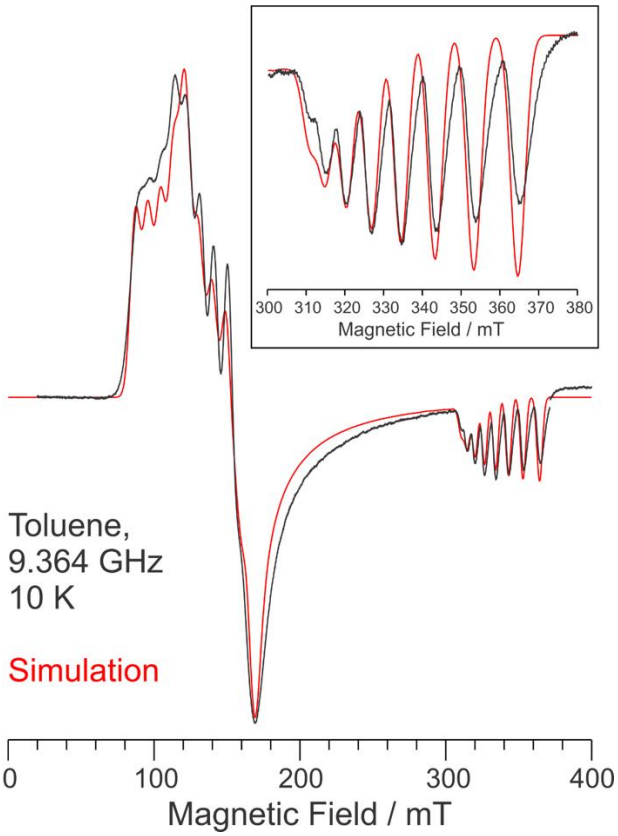

Figure 3. Experimental X-band EPR spectra of **CoCl** as a toluene solution (black trace) recorded at 10 K (9.364 GHz). Simulation of the solution spectrum (red trace) uses: S' = 1/2, **g′** = [5.64, 4.60, 1.97] (defined simply by g'_{max}, g'_{mid}, g'_{min}), **A′**(^{59}Co) = [700, 400, 210] MHz (**A′** collinear with **g′**), W (half-width at half-maximum (hwhm), Gaussian) = 320, 280, 60 MHz. The inset shows an expansion of the $g'_{\|}$ region for the solution with the same simulation parameters.

The situation with **$CoCH_3$** is quite different. In this case, conventional EPR spectra were very difficult to obtain due to the extreme air sensitivity of the complex, which required the use of sealed tubes, precluding Q-band measurements. Nevertheless, it was clear that **$CoCH_3$** exhibited spectra characteristic of an S = 3/2 system with D < 0 (i.e., m_S

= ±3/2 ground state). Such X-band spectra are distinctive in that they exhibit a very large $g'_{\|}$ (i.e., at very low field, usually with resolved ^{59}Co hyperfine coupling) and a very small $g'_{\perp}$ (i.e., at very high field – by X-band standards). An example of such an EPR spectrum was reported for the three-coordinate Co^{II} NHC complex [$Co(CH_2SiMe_3)_2$(IPr)] (IPr = 1,3-bis(2,6-diisopropylphenyl)imidazol-2-ylidene), which gave **g′** = [8.85, 1.89, 1.10] with well-resolved ^{59}Co hyperfine coupling at low field (splitting of 17.7 mT; the spectrum was not simulated).[102] Figure 4 presents the low field region of the X-band EPR spectrum of **CoCH$_3$**. In contrast to the NHC complex,[102] no features attributable to $g'_{\perp}$ (g'_{mid} or g'_{min}) were definitively observed (see Figure S5). These g' value turning points may lie beyond the maximum field of the X-band spectrometer (~600 mT, $g' \approx 1.1$). Nevertheless, both g'_z and A'_z (A'_{max}) are reasonably well determined and give values close to those reported for the NHC complex (17.7 mT[102] versus an average splitting of 16.5 mT in **CoCH$_3$**). If we assume g_z = 2.85, based on the magnetometry (see below), then the real hyperfine coupling, $A_z \approx$ (1850 MHz)(2.85/8.5) = 620 MHz, as opposed to 435 MHz using g_z = 2.0. The real value for the NHC complex is likely similar. For further comparison, four-coordinate, homoleptic Co^{II} complexes, [$Co(OAsMePh_2)_4$](ClO_4)$_2$ [98] and [$Co(NH_2CSNH_2)_4$](NO_3)$_2$,[103] studied as powders doped into their corresponding Zn^{II} hosts exhibited X-band spectra similar to that seen for **CoCH$_3$**, with neither clearly providing g'_{mid} or g'_{min} values. The arsine oxide complex yielded $g'_z \approx 8.1$ and A'_z = 1586 MHz;[98] the thiourea complex was not analyzed quantitatively, but the resolved splitting appears to be ~20 mT,[103] and thus consistent with the other cases. The key qualitative finding from conventional EPR of **CoX** is that the sign of D is opposite between **CoCl** ($D > 0$) and **CoCH$_3$** ($D < 0$), which is quantitatively analyzed in the computational section below.

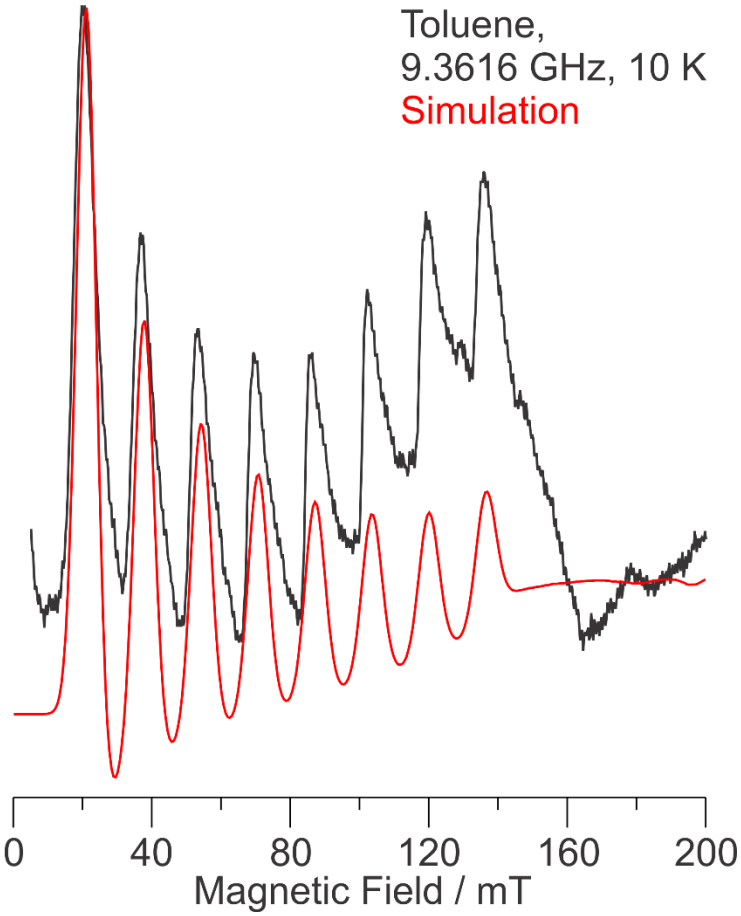

Figure 4. Experimental X-band EPR spectrum of **CoCH$_3$** in frozen toluene solution (black trace) recorded at 10 K (9.3616 GHz). Simulation (red trace) uses: S' = 1/2, **g′** = [8.50, 1.2, 1.0] (defined simply by g'_{max}, g'_{mid}, g'_{min}; the last two g' values are essentially arbitrary), **A′**(^{59}Co) = [1950, 400, 400] MHz (**A′** collinear with **g′**), W (half-width at half-maximum, Gaussian) = 400, 500, 500 MHz. It is not possible to match exactly the experimental lineshape, but the hyperfine splitting pattern is reproduced by the simulation. As with g', the last two A' components and linewidths are arbitrary as there is no reliable experimental data for their determination (see also Figure S5).

ENDOR Spectroscopy.

As described above, due to their previous investigation by conventional EPR,[4] no such experiments were undertaken here on **FeX**. As also indicated above, conventional X-band EPR spectroscopy in frozen solution was fruitful for **CoX**, although Q-band EPR was not feasible for **CoCH$_3$**. **CoCl**, in contrast, could be studied by Q-band EPR (Figure S4) and thus by ENDOR spectroscopy at this frequency as well. Signals due to ^{1}H in **CoCl** are seen using CW 35 GHz ENDOR as shown in Figure S6 and discussed in Supporting

Information. More important are the ^{14}N signals from the nacnac ligand. Pulsed (Davies) ENDOR spectra for **CoCl** recorded across its EPR envelope are shown in Figure 5. These spectra could be analyzed quantitatively by ENDOR simulation using $S' = 1/2$ and $\mathbf{g'}$ as above, now also with $\mathbf{A'}(^{14}\text{N})$ and $\mathbf{P}(^{14}\text{N})$ (the nqc is a purely nuclear interaction, involving no electronic spin terms, so that it is determined regardless of whether S or S' is used). The simulations assume that the two nacnac ^{14}N are equivalent, which is true in the solid-state crystal structure. That the X-band EPR spectra in a powder and in solution are the same (see Figure S3) suggests that the two ^{14}N are equivalent in solution as well. Such an assumption may be an oversimplification given that ^{14}N ENDOR can, in ideal cases (e.g., single crystal studies of hemes / porphyrins that included ^{15}N-enrichment[104, 105]) reveal slight magnetic differences among structurally equivalent ligands. The situation with **CoCl** is far from this ideal not only in lacking ^{15}N-enrichment and single-crystals, but also having severe disadvantages with respect to the desirable , yet common, situation of $S = 1/2$ with hfc small relative to EPR linewidth: the high-spin state of **CoCl** so that the g/g' factor operates but is not accounted for, and the ^{59}Co hfc, which complicates the orientation selection ability of ENDOR[106, 107] by making a given g' (i.e., the field at which ENDOR is recorded) shifted/split by the ^{59}Co hfc making the EPR linewidth used for simulation less meaningful. Nevertheless, a reasonable reproduction of the ^{14}N ENDOR pattern is achieved as shown in Figure 5. The fit parameters are: $\mathbf{A'}(^{14}\text{N})$ = [11.8, 21.4, 7.3] MHz, $\mathbf{P}(^{14}\text{N})$ = [+1.26, -0.80, -0.46] MHz. The $\mathbf{A'}(^{14}\text{N})$ can be converted to $\mathbf{A}(^{14}\text{N}) \approx$ [11.8(2.580/5.68), 21.4(2.585/4.70), 7.3] MHz = [5.4, 11.8, 7.1] MHz, so $A(^{14}\text{N})_{iso} \approx 8.2$ MHz. Despite the widespread use of the nacac ligand platform, this represents, to our knowledge, the first determination of ^{14}N hfc for the β-ketiminate donors. For comparison, such data for more "ENDOR-friendly" $S = 1/2$ systems such as (nacnac)CuCl[108] and (nacnac)NiL, L = CO, thf,[109] would be useful; especially the Ni^{I} complexes that are absent any non-^{1}H hfc except from ^{14}N. The closest comparison that can be made to the present $A(^{14}\text{N})_{iso}$ value is the result of Tierney and co-workers[110] who found for Tp_2Co that A(pyrazolyl-2-^{14}N)$_{iso}$ = 11.8 MHz. The electronic structure of 6-coordinate Co(II) is much more complicated than that for **CoX** due to unquenched orbital angular momentum,[110-113] but this $A(^{14}\text{N})_{iso}$ value is in the range of that observed here. Also relevant is the work of Walsby et al. on a Co^{II}-substituted Zn^{II} protein, Finger 3 of Transcription Factor IIIA, [97] which has a Cys_2His_2 coordination site. They found $A(^{14}\text{N})$ = 7.2 MHz, close to what is seen here, and they point out that this value is close to that seen

for histidine imidazole N coordinated to Cu^{II}, when the appropriate scaling factor of $2S = 3$ is used:[97] $A_{S=1/2} = A_{S=3/2}(3) = 24$ MHz in our case.

To contextualize the observed ^{14}N nqc, we turn to the metalloporphyrin literature, namely single-crystal ENDOR studies by Brown and Hoffman on Cu^{II}(TPP) (TPP = 1,5,10,15-tetraphenylporphyrin)[114] and by Scholes et al. on aquometmyoglobin (Fe^{III}(PPIX), $S = 5/2$).[104] For Cu(TPP) (doped into a Zn(TPP)(H_2O) host), $\mathbf{P}(^{14}N)$ = [–0.619, +0.926, (–0.307)] MHz[114, 115] For myoglobin, the average of the four heme nitrogen donors gave $\mathbf{P}(^{14}N)$ = [–0.77, +1.04, –0.27] MHz. These values for porphyrin pyrrole N donors are not only close to each other, despite the coordinated metal ions' size, charge, and spin state, but in the same range as that observed here for β-diketiminate N donors. Note that, unlike in these single-crystal studies, we have less certainty as to the relative orientations of the **g**, **A**, or **P** tensors with respect to each other or to the molecular frame of reference, although we make assumptions based on the coordinate system in Figure 1.

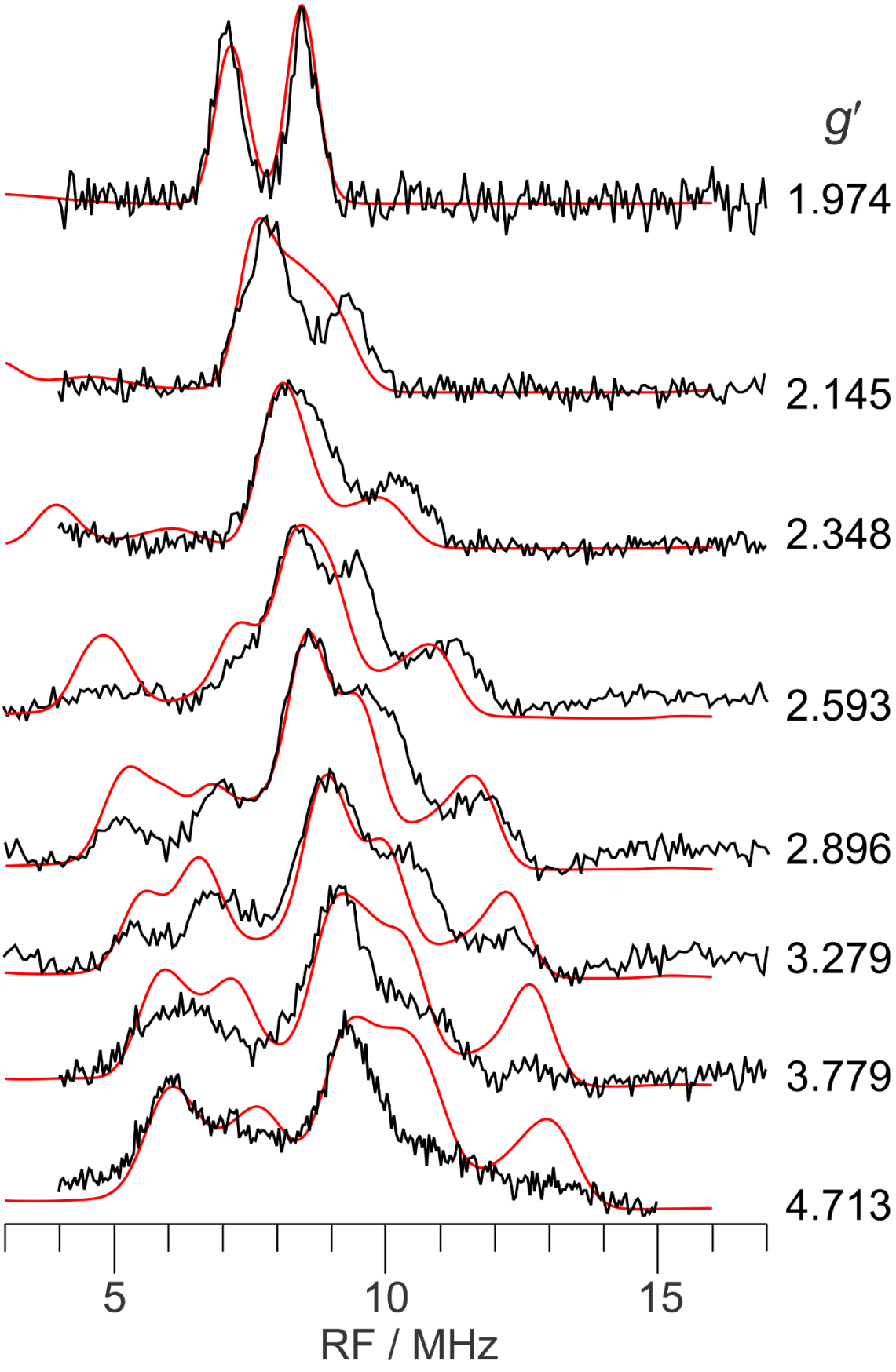
g′
1.974
2.145
2.348
2.593
2.896
3.279
3.779
4.713
5
10
15
RF / MHz

Figure 5. Pulsed 35 GHz ^{14}N ENDOR spectra of **CoCl** in toluene frozen solution (black traces) with simulations (red traces). Experimental parameters: temperature, 2 K; microwave frequency, 34.846 GHz; Davies sequence with t_π = 80 ns, τ = 600 ns, t_{rf} = 15 μs with random hopping of rf, repetition rate, 20 ms; typically 10 scans. Simulation parameters: S' = 1/2, **A′**(^{14}N) = [12.2, 20.6, 7.1] MHz, **P**(^{14}N) = [+1.26, -0.80, -0.46] MHz, W_{NMR} = 0.5 MHz, W_{EPR} = 800 MHz (both Gaussian, hwhm). The broad, isotropic EPR linewidth is an attempt to model the ^{59}Co hfc. The **A′**(^{14}N) and **P**(^{14}N) tensors are each rotated by Euler angle α = 130° with respect to the **g′** tensor so that the $(A',P)_z$ (out-of-plane) direction remains along g'_z, but $(A',P)_{x,y}$ (in-plane) is along the N-Co bond (see Figure 1).

Magnetometry. In contrast to conventional EPR spectroscopy, magnetometry (here DC susceptibility and VTVH-magnetization) can in principle directly provide the magnitude of D. We collected the dc magnetic susceptibility data for both **CoCl** and **CoCH$_3$**, which are presented in the insets of Figure 6. For **CoCl**, the 300 K $\chi_M T$ value of 3.0 cm^{3}K/mol supports a g_{iso} value of 2.52 and is consistent with the anisotropic g-values extracted from EPR spectroscopy (EPR analysis supports a g_{iso} value of 2.39). Similarly, **CoCH$_3$** displays a 300 $\chi_M T$ value of 2.62 cm^{3}K/mol, consistent with g_{iso} = 2.36. For both **CoCl** and **CoCH$_3$**, their $\chi_M T$ values begin to decrease below 150 K, ultimately reaching values of 1.97 cm^{3}K/mol (**CoCl**) and 2.06 cm^{3}K/mol (**CoCH$_3$**) at 2 K. An initial estimation of their axial zero-field splitting parameters (D) was determined by fitting their dc susceptibility data (Table 1). For **CoCl**, this fitting yielded D = +59(3) cm^{-1} and $g_\perp$ and $g_\parallel$ values of 2.65 and 2.16, respectively. For **CoCH$_3$**, this fitting yielded D = –91(5) cm^{-1} and $g_\perp$ and $g_\parallel$ values of 2.02 and 2.88, respectively. To gain a better estimate of the spin Hamiltonian parameters, we collected and fit the variable temperature, variable field (VTVH) magnetization data for **CoCl** and **CoCH$_3$** (see Figure 6 and S11). Our best simulations afforded D = +55(2) cm^{-1}, and $g_\perp$ and $g_\parallel$ values of 2.62 and 2.08, respectively, for **CoCl**, and D = –91(5) cm^{-1}, and $g_\perp$ and $g_\parallel$ values of 2.17 and 2.85, respectively, for **CoCH$_3$**. These bulk magnetization data qualitatively agree with the analysis of the EPR spectra for **CoCl** and **CoCH$_3$**, whose spectra were consistent with **CoCl** possessing a large and positive D value, while **CoCH$_3$** possesses a large and negative value of D. More quantitatively, use of these g values from magnetization in the perturbation theory equations[91, 95] gives for **CoCH$_3$** a viable range from $g'_x = g'_y = 0$, $g'_z = 8.55$ for $E/D = 0$ to $g'_x = 0.50$, $g'_y = 0.54$, $g'_z = 8.50$ for $E/D = 0.08$. This result suggests the futility of observing $g'_\perp$ for **CoCH$_3$** by conventional EPR.

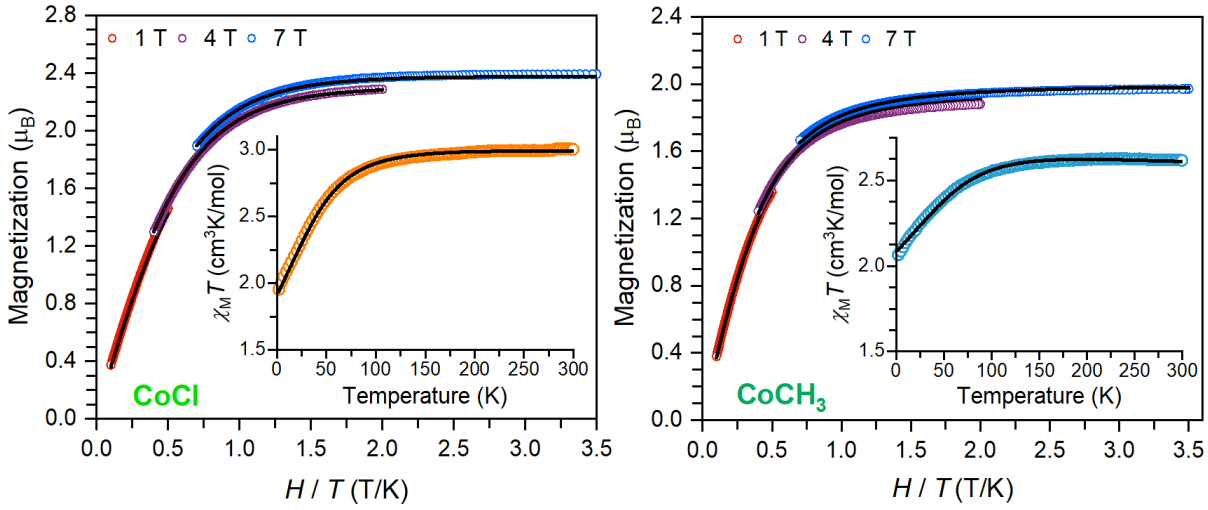

Figure 6. Variable temperature, variable field (VTVH) magnetization data of **CoCl** (left) and **CoCH$_3$** (right) each collected in the temperature range of 2 – 10 K and at fields of 1, 4, and 7 T. The 0.1 T dc susceptibility for both compounds are presented in the insets. The black traces are best fits to each of the VTVH magnetization and dc susceptibility data (see Table 1 for fit parameters). Complete VTVH magnetization data are given in Supporting Information (Figure S11).

Far-infrared magnetic spectroscopy (FIRMS). FIRMS allows direct evaluation of the zfs in an $S = 2$ system such as found for **FeCl** and **FeCH$_3$** which includes determination of the zfs rhombicity.[94] Measurement of **FeX** powder samples with no applied field gives spectra with two absorption peaks, which are observed at 108.3 and 120.6 cm^{-1} for **FeCl** and at 107.2 and 114.5 cm^{-1} for **FeCH$_3$**. Note that other signals are observed for which the frequency is independent of the magnetic field, and thus these are attributed to vibrational bands (phonons). The spectra are presented in Figure 7 (top), with additional spectra in Supporting Information (Figures S7 – S10). In an $S = 2$ system with $D < 0$ and $E \neq 0$ (assumed $E < 0$, to correspond to the sign of D), these transition energies correspond to ~3$|D - E|$ and ~3$|D + E|$, respectively (see Figure 2). The spin Hamiltonian parameters for the four studied complexes are given in Table 1.

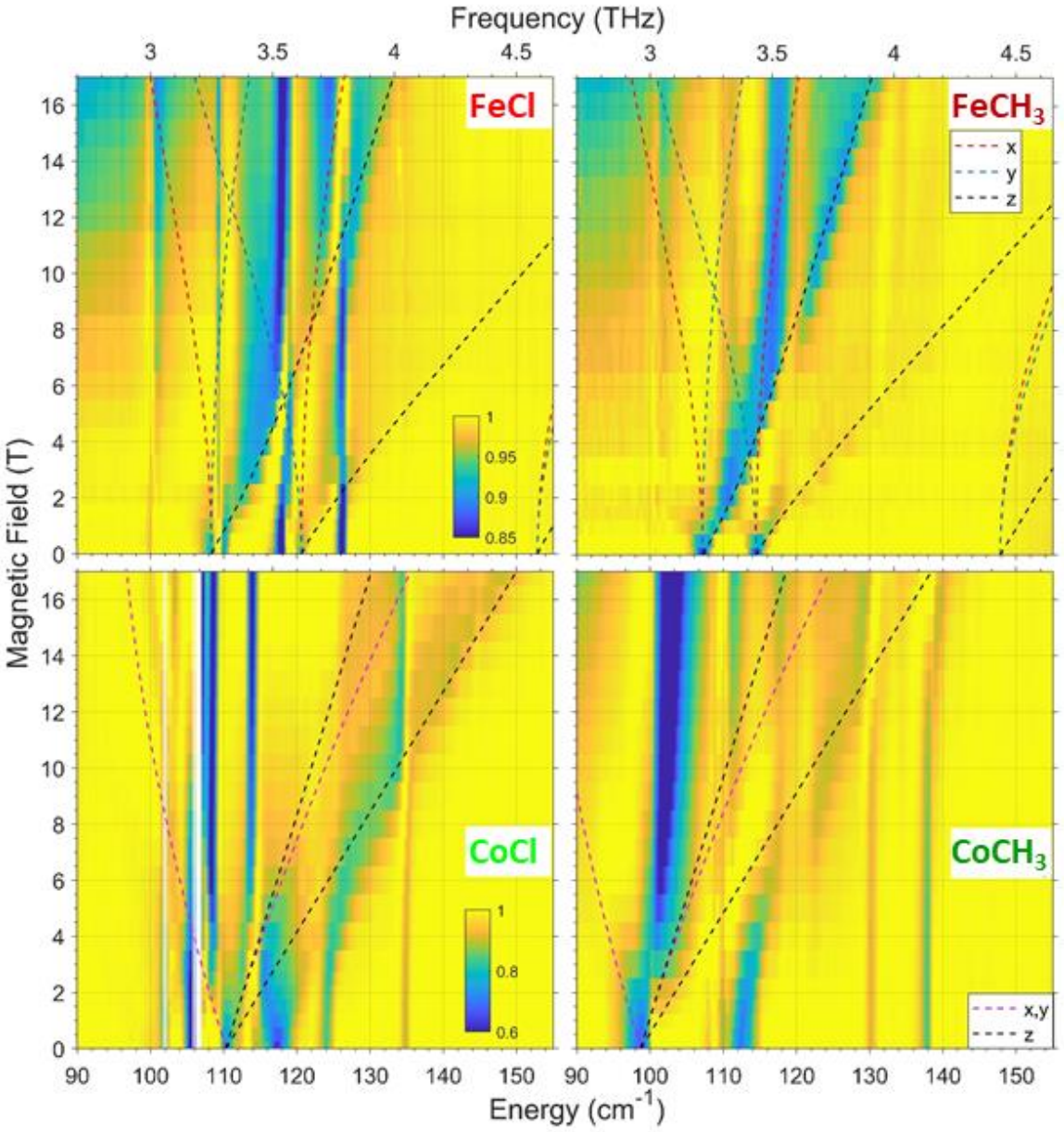

Figure 7. FIRMS color maps for **FeCl** (top, left), **FeCH**$_3$ (top, right), **CoCl** (bottom, left), and **CoCH**$_3$ (bottom, right) each collected at 5.5 K. The magnitude of the field-induced variation in the transmission spectrum is depicted in a color scale (see inset in left panels), which is same within each **FeX** and **CoX** pair of compounds. The part of the spectrum with large experimental error (>3%) is indicated in white. For **FeX**, the dashed lines indicate spectral positions of the magnetic resonance with the external magnetic field aligned along the zfs (**D**) tensor *x* (red lines), *y* (blue), and *z* (black) principal axes; for **CoX**, only axial fits were used so magenta lines indicate the field aligned along the *x*,*y*

(perpendicular, ⊥) direction, with black lines again for the field aligned with *z* (parallel, ||). These lines were generated visually and not by any automated fitting routine. Due to spin-phonon coupling, the non-magnetic transitions (phonons) show up as vertical lines and are often quite intense (dark blue). More traditional in appearance single-beam transmission far-IR spectra are presented in Figures S7 and S8, which respectively show the effects of applied field and of air exposure. Figure S9 presents color maps for each complex on a wider energy range (80 – 220 cm^{-1}) and also shows the effects of air exposure. Figure S10 shows an attempt to identify the $|S, m_S\rangle = |2, \pm2\rangle \rightarrow |0\rangle$ transition ($\Delta m_S = 2$; see Figure 2) in **FeCH$_3$**.

In the case of an $S = 3/2$ spin system, such as **CoCl** and **CoCH$_3$**, information on the rhombicity of the zfs (**D**) tensor cannot be obtained, only the zero-field energy gap between the $m_S = \pm1/2$ and $\pm3/2$ Kramers doublets (see Figure 3), here denoted $2D^*$ (alternatively as Δ). These spectra are presented in Figure 8 (bottom), with additional spectra in Figures S7 – S9. Although large field-induced changes in the transmission are observed for both **CoX** compounds (see Figure S7), $2D^*$ values are challenging to extract because all the spectra are affected by strong spin-phonon coupling effects.[116] As a result, the ground state in these complexes is vibronic (crystal field plus phonon (vibrational mode)), therefore resulting in a hybridization of the crystal field levels leading to a complex FIRMS pattern compared to what would be expected using a simple $S = 3/2$ spin Hamiltonian model, namely a single absorption at $2D^*$ (Figure 2), which would split in applied field due to the Zeeman effect. Nevertheless, the complex FIRMS pattern in Figure 7 can be interpreted by inspection of absorption peaks in the FIR transmission spectra (e.g., Figures S7 and S8) as well as the fields/frequencies where the more pronounced phonon peaks (i.e., dark vertical lines) exhibit crossing behavior, namely a drop in intensity due to a spin-phonon interaction at that point. An example is seen at ~106 cm^{-1} and ~4 T for **CoCl**. From this analysis we suggest the inter-doublet energy gap (see Figure 2) to be $2D^* = 110.4$ cm^{-1} for **CoCl**, which agrees well with the value from magnetometry ($2D^* = 114(4)$ cm^{-1}; see Table 1). **CoCl** exhibits an additional, nearby feature at 117.2 cm^{-1} that might also be due to magnetic resonance absorption, which also agrees with magnetometry and calculations (see below). The situation for **CoCH$_3$** is more ambiguous. There are zero-field absorptions at 98.8 cm^{-1}, 112 cm^{-1}, 137 cm^{-1}, and 169.3 cm^{-1} (see Figures S8 and S9 for the higher energy region). Among these, we favor assignment of the band at 98.8 cm^{-1} to $2D^*$, as given in Table 1, but none of the others can

be totally ruled out. Thus, FIRMS suggests that for **CoCH$_3$**, –85 cm^{-1} ≤ D ≤ –50 cm^{-1}, with the negative sign based on magnetometry and conventional EPR.

Table 1. Spin Hamiltonian parameters for **MX** complexes with CASSCF/NEVPT2 + SOC calculated parameters.

Complex, technique	D (cm^{-1}), E (cm^{-1}), $\|E/D\|$	[g_x, g_y, g_z], g_{iso}	g'_x, g'_y, g'_z [e]
FeCl			
FIRMS	–38.05 ± 0.1, –2.05 ± 0.1, 0.054	[2.2, 2.2, 2.5], 2.3	---
Conventional EPR [a]	---	---	---, ---, 10.9
Calculated	–51.5, -2.1, 0.04	[1.90, 2.01, 2.90], 2.27	
FeCH$_3$			
FIRMS	–36.92 ± 0.5, –1.22 ± 0.5, 0.033	[2.2, 2.2, 2.5], 2.3	---
Conventional EPR [a]	---	---	---, ---, 11.4
Calculated	–50.1, -2.0, 0.04	[1.91, 2.03, 2.89], 2.28	
CoCl			
FIRMS [b]	55.2 ± 0.2, 0, 0	2.5	---
Magnetometry [c]	+55 ± 2, 0, 0	[2.62, 2.62, 2.08], 2.44	5.24, 5.24, 2.08
Conventional EPR [d]	> 0, ---, 0.065	---	4.66(4), 5.66(2), 1.965(5)
Calculated [e]	+65.5, 4.6, 0.07	[2.79, 2.85, 1.95], 2.53	4.98, 6.27, 1.92
CoCH$_3$			
FIRMS [b]	–49.4 ± 0.2, 0, 0	2.5	---
Magnetometry [c]	–91 ± 5, 0, 0	[2.17, 2.17, 2.85], 2.40	0, 0, 8.55
Conventional EPR [d]	< 0, ---, ---	---	---, ---, 8.50
Calculated [e]	–122.4, -4.9, 0.04	[1.05, 2.09, 3.59], 2.24	0.13, 0.24, 10.75

[a] Taken from Andres et al.[4] using X-band EPR with parallel mode detection.

[b] Only the D^* parameter and $g'_{\|}$ can be evaluated from our experimental FIRMS data. For **CoCl**, the most favorable assignment for D is given, but the range 55 $cm^{-1} \leq |D| \leq 59$ cm^{-1} covers both possible assignments. In contrast, FIRMS for **CoCH$_3$** is especially complicated by spin-phonon interactions. The most favorable assignment for D is given, but the range ~50 $cm^{-1} \leq |D| \leq$ ~85 cm^{-1} encompasses all possible assignments. The positive sign of D for **CoCl** and negative sign for **CoCH$_3$** is inferred from their X-band EPR spectra, and is corroborated by magnetometry and calculations.

[c] The values given are those from fits of VTVH magnetization data. Fits of DC susceptibility measurements gave for **CoCl**, $D = +59(3)$ cm^{-1}, $g_{\perp} = 2.65$, $g_{\|} = 2.16$ ($g_{iso} = 2.49$); for **CoCH$_3$**, $D = -91(5)$ cm^{-1}, $g_{\perp} = 2.02$, $g_{\|} = 2.88$ ($g_{iso} = 2.31$). Perturbation theory equations[91, 95] give $g'_{x,y,z}$ values ($S' = 1/2$) derived from $g_{x,y,z}$ values obtained from fits of magnetometry using $S = 3/2$. Using the parameters from DC susceptibility the results are $\mathbf{g}' = [5.30, 5.30, 2.16]$ for **CoCl** and $g'_z = 8.64$ for **CoCH$_3$**.

[d] X-band EPR provides $|E/D| = 0.065$ for **CoCl** from the splitting of the $g'_{\perp}$ feature (see text) using the perturbation theory equations. The range of g' values comprises both X- and Q-band EPR measurements as well as different sample preparations. This determination is impossible for **CoCH$_3$** as only the $g'_{\|}$ feature is observed.

[e] The g' value ordering is taken here to match experiment using the conventional assignments in EPR and magnetometry where $g_{\|} \equiv g_z$ and $g_{\perp} \equiv g_{x,y}$.

Electronic absorption spectra. The electronic absorption spectra of **FeX** and **CoX** recorded at room temperature in toluene solution are shown in Figure 8 on an energy (wavenumbers, cm^{-1}) scale. These spectra are shown on a wavelength scale in Figures S1 and S2 respectively for **FeX** and **CoX**. A simple ligand field theory (LFT) discussion of these spectra is given below followed by a definitive explanation using quantum chemical theory (QCT), specifically time-dependent density functional theory (TD-DFT).

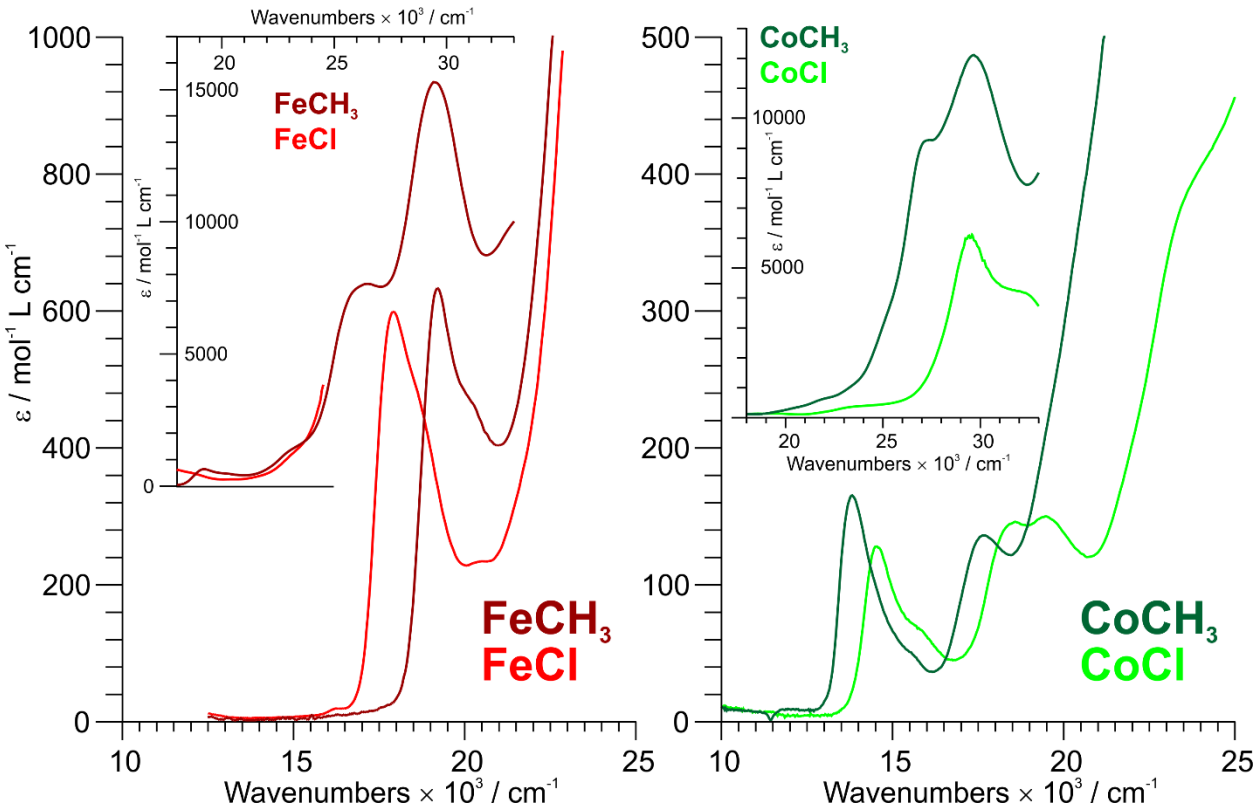

Figure 8. Electronic absorption spectra (main figure, Vis-NIR region; inset UV-Vis region) on a wavenumber (energy) scale of **FeX** (left panel) and **CoX** (right panel) recorded at room temperature in toluene solution. Complete UV data are unavailable for **FeCl**.

Ligand field theory (LFT): optical spectra and zfs. A quantitative analysis of the electronic structure of the **MX** series is provided using QCT in the following section, but we first discuss classical LFT because it is still instructive. We begin with an idealized trigonal planar geometry as shown in Figure 1 (left panel), Even in this relatively high D_{3h} symmetry the number of states is very large as shown in Table S1 (Supporting Information). To explain qualitatively the electronic absorption spectra of the complexes we employ only spin-allowed d-d transitions as their possible origin. Considering first the **FeX** complexes (Figures 8 (left) and S1), there are visible absorption bands at 559 nm (17 890 cm^{-1}; ε = 1700 mol^{-1} L cm^{-1}) for **FeCl** and at 517 nm (19 340 cm^{-1}; ε = 590 mol^{-1} L cm^{-1}) for **FeCH3**. In D_{3h} symmetry, with *only* σ-bonding and ignoring the JTE, the ground state is $^5E''$, with the β electron of d^6 in d_{xz}, d_{yz}) with the first excited state being $^5A_1'$ (β electron in d_{z^2}) and then $^5E'$ (β electron in $d_{xy}, d_{x^2-y^2}$) followed by the numerous triplet and singlet excited states. The transition $^5E'' \rightarrow {}^5E'$ is dipole allowed with *z* polarization

($^5E'' \rightarrow {}^5A_1'$ is forbidden; $^5A_1' \rightarrow {}^5E'$ is dipole allowed with *xy* polarization) so this could be the origin of the visible band. However, this assignment would require unreasonably large bonding parameters (ε_σ = 15 902 and 19 191 cm^{-1} for **FeCl** and **FeCH$_3$**, respectively) so that a simple σ-only bonding model disfavors a d-d assignment for the visible band in **FeX**. Another option is to include π-bonding, which could be either donating or accepting. This is a serious complication in the real **FeX** complexes as the methyl ligand would have no π-bonding, the chlorido ligand would be cylindrical ($\varepsilon_{\pi-s} = \varepsilon_{\pi-c}$), and π-bonding involving the nacnac with its sp^2 nitrogen ligands would likely be only out-of-plane ($\varepsilon_{\pi-s} = 0$, $\varepsilon_{\pi-c} \neq 0$). To maintain D_{3h} symmetry in the present model, we use the same π-bonding for all three ligands. In plane π-bonding could be included to lower ε_σ (e.g., $\varepsilon_{\pi-s} = 0.2\varepsilon_\sigma$ gives ε_σ = 13 572 cm^{-1} for **FeCH$_3$**), but its value is still too large. Out-of-plane π-bonding could instead be included, which has the advantage that with sufficient π-donation, the ground state becomes $^5A_1'$, as in Figure 1 (left). The problem is that this effect brings the $^5E'$ excited state lower in energy – further from the observed band energy making fitting even less viable. Given the total failure of the trigonally symmetric D_{3h} model, it is not worthwhile to modify it to closer to the real, C_{2v} symmetry. We conclude that the visible band in **FeX** is likely a charge transfer (CT) band (whether metal-to-ligand (MLCT) or ligand-to-metal (LMCT) is uncertain), which is supported by its relatively high molar absorption coefficient.

In the **CoX** complexes (see Figures 8 (right) and S2) there are visible bands at 514 and 540 nm (19 455 and 18 520 cm^{-1}; both $\varepsilon \approx 150$ mol^{-1} L cm^{-1}) and at 635 nm (15 750 cm^{-1}; sh) and 687 nm (14 555 cm^{-1}; ε = 130 mol^{-1} L cm^{-1}) for **CoCl** and at 565 nm (17 700 cm^{-1}; ε = 130 mol^{-1} L cm^{-1}) and at 640 nm (15 625 cm^{-1}; shoulder (sh)) and 725 nm (13 790 cm^{-1}; ε = 160 mol^{-1} L cm^{-1}) for **CoCH$_3$**. These lower molar absorption coefficients support the assignment of these bands as being d-d transitions. In contrast to **FeX**, the quartet electronic states of **CoX** are more complicated. The free-ion ^4F splits into $^4A_2'$, $^4E''$, $^4A_1''$ and $^4A_2''$ (degenerate in D_{3h}), and $^4E'$, with the states derived from ^4P, $^4A_2'$ and $^4E''$, higher in energy. Table S2 (Supporting Information) illustrates the states for idealized **CoX** considering *only* σ-bonding (ε_σ = 7000 cm^{-1}) and with Racah parameters at 70% of their free-ion values.[117] Using this very simplified, idealized model, one can more quantitatively rationalize the observed electronic transitions for both **CoCl** and **CoCH$_3$** as being viable as d-d transitions, in contrast to the situation for **FeX**. This is done using three possible sets of assignments: a) the lower energy visible band corresponds to $^4A_2' \rightarrow {}^4A_1''$,$^4A_2''$ and the higher energy band to $^4A_2' \rightarrow {}^4E'$ (both allowed); b) the lower to $^4A_2'$

$\rightarrow$ ^{4}E′ and the higher to ^{4}A$_2$′ $\rightarrow$ ^{4}E″(P) (forbidden in D_{3h}, but allowed in the lower real symmetry); and c) the lower to ^{4}A$_2$′ $\rightarrow$ ^{4}A$_1$″,^{4}A$_2$″ and the higher to ^{4}A$_2$′ $\rightarrow$ ^{4}E″(P). The transitions ^{4}A$_2$′ $\rightarrow$ ^{4}E″(F) and ^{4}A$_2$′ $\rightarrow$ ^{4}A$_2$′(P) would be respectively too low and too high in energy to be observed (see Table S2) as well as being dipole forbidden in D_{3h}. Fits were made using these three models with variable ε_σ and with the Racah *B* parameter either fixed at 70% or variable (Racah *C* in this model is large since doublet states were ignored). As expected, fits with fixed *B* were not very successful, yet model (b) agreed reasonably well with experimental data. Allowing *B* to vary led to perfect fits for both models (a) and (b); however, the fit values for model (a) were less realistic in that values for *B* were low and for ε_σ very high. In contrast, model (b) gave perfect fits with reasonable values for both parameters. The results are given in Table S3 (Supporting Information). LFT thus provides an idea as to the origin of the electronic transitions observed for the **MX** and in particular **CoX** complexes.

The next step is to use the idealized C_{2v} geometry with the above bonding parameters as a guideline and explore the ability of LFT to model the zfs. Use of the actual ∠X-Co-N = 130.6 ± 0.3° and ε_σ(X) ≠ ε_σ(N) (ε_π(X,N) = 0) successfully fits the absorption bands (Table S4) with the *B* value and bonding parameters still reasonable. For both **CoCl** and **CoCH$_3$**, ε_σ(X) > ε_σ(N). This is expected for the methyl anion, and in the case of chloride, this parameter also includes π-donation that is not specifically accounted for so as to avoid overparameterization. We acknowledge that π-bonding involving the chloride is key in that it removes the degeneracy of the and d_{yz} orbitals, as discussed in the QCT section, but we cannot quantify it here based on the available data. The results of these fits can then be used with inclusion of SOC to attempt to reproduce the spin Hamiltonian parameters. In this case, the Racah *C* parameter and the SOC constant ζ are both chosen to have the same reduction from their free-ion values as the fits obtained for *B*; though this is an oversimplification, it is useful for illustration. For **CoCl**, this model gives **g′** = [5.73, 2.84, 1.76] and 2*D** = 41 cm^{-1}, ignoring the small rhombicity gives *D* ≈ 20 cm^{-1} – lower than the FIRMS value (Table 1), but this could be increased by an larger ζ value.[118] The sign is positive based on the spin magnitudes (lowest doublet is $\langle S_z^2 \rangle$ = ±0.44; the higher doublet has $\langle S_z^2 \rangle$ = ±1.43). For **CoCH$_3$**, use of ζ = 425 cm^{-1} gives **g′** = [7.02, 1.76, 1.27] and 2*D** = 74 cm^{-1}. Surprisingly, although the **g′** tensor is not unreasonable, giving one large and two small components, the spin magnitudes (lowest doublet $\langle S_z^2 \rangle$ = ±0.32; higher doublet $\langle S_z^2 \rangle$ = ±1.31) do not support a negative *D* value.

Quantum chemical theory (QCT): Time-dependent DFT (TD-DFT). The above LFT section discusses the electronic absorption spectra of the **MX** series. For the **FeX** complexes, it was proposed that the observed bands were due to transitions that involved the ligands, rather than d-d transitions that could be modelled using LFT. As shown in Figures S12 and S13, this is indeed the case. Figure S12 (bottom) presents the calculated spectra for the entire **MX** series so that it is readily apparent that the **CoX** complexes exhibit d-d transitions in the visible-NIR region, while the **FeX** complexes lack these. In particular, the energy of the visible band at 559 nm (17 900 cm^{-1}) in **FeCl** (Figure 8) likely corresponds to the lowest energy LMCT transition calculated by TD-DFT (Figure S12) at 20 418 cm^{-1} (Figure S13). For **$FeCH_3$**, no such distinct band is calculated, but the LMCT shoulders extend into the region where the band at 517 nm (19 340 cm^{-1}; Figure 8) is observed. For the **CoX** complexes, the visible bands were assigned to d-d transitions and analyzed approximately using LFT, which description is confirmed by TD-DFT. The longer wavelength, more intense, visible bands at 687 nm (14 555 cm^{-1}) and 725 nm (13 790 cm^{-1}) for **CoCl** and **$CoCH_3$**, respectively, are d-d in character, with the electron density changes (see Figure S13) entirely on the Co^{II} center. Their energies are matched by calculated bands (Figure S12) at 15 707 cm^{-1} and 13 426 cm^{-1} respectively for **CoCl** and **$CoCH_3$**. Additionally, the shorter wavelength, less intense, pair of visible bands for **CoCl** at 514 nm (19 455 cm^{-1}) and 540 nm (18 520 cm^{-1}) are matched by a calculated band at 19 421 cm^{-1} (see Figure S12, which gives further discussion on this point).

Quantum chemical theory (QCT): ab initio calculated g*-values and zfs.* Complete active space self-consistent field (CASSCF) calculations were performed on the series of complexes using the atomic coordinates derived from previously reported x-ray structures. The results of these ab initio calculations were mapped onto a ligand field Hamiltonian using the ab initio ligand field theory (AILFT) procedure.[119] The AILFT orbital level diagram is presented in Figure 9 and the relevant parameters (3d single electron orbital energies, Racah and ζ values) are listed in Table 2. The Racah parameters determined by AILFT are greater than their free-ion values (by ~15 – 20% in *B* and 2 – 6% in *C*),[117] so they should not be used in absolute sense, but are useful in comparison among the **MX** series in terms of showing that each pair of complexes with the same metal ion has essentially the same parameters despite the difference between X = Cl and CH_3. The SOC constants so determined are ~93% of the free-ion values across all four complexes.

Table 2. CASSCF + SOC derived AILFT parameters (in cm^{-1}) for **MX** series.

Compound	3d Orbital Energies $\left(d_{yz}, d_{z^2}, d_{xz}, d_{x^2-y^2}, d_{xy}\right)$	ζ [a]	*B*, *C*, (*C*/*B*) [b]
FeCl	0, 96, 2391, 4512, 11556	395.6	1087, 4125, (3.80)
$FeCH_3$	0, 87, 2376, 5288, 10862	393.4	1077, 4123, (3.83)
CoCl	0, 58, 1935, 4138, 11049	504.4	1146, 4336, (3.78)
$CoCH_3$	0, 97, 1875, 5128, 10248	502.2	1138, 4336, (3.81)

[a] These can be compared to the free-ion values: 427 (Fe^{II}) and 533 (Co^{II}).[120]

[b] These can be compared to the free-ion values: 897.1 (*B*), 3877.1 (*C*), 4.32 (*C*/*B*) (Fe^{II}) and 988.6 (*B*), 4214.3 (*C*), 4.26 (*C*/*B*) (Co^{II}).[117]

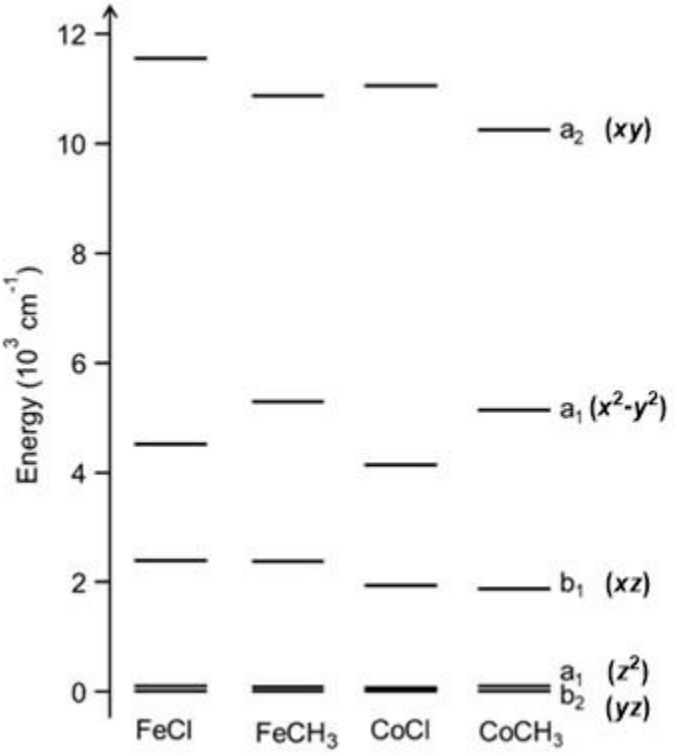

Figure 9. AILFT *d*-orbital energy level diagram derived from CASSCF calculations for **FeCl**, **$FeCH_3$**, **CoCl**, and **$CoCH_3$**. This quantitative ordering is the same as that shown qualitatively in Figure 1, except therein the splitting between the d_{yz} and d_{z^2} orbitals is

increased for illustrative purposes with d_{z^2} lowest as in Andres et al. [4] This apparent discrepancy is the consequence of non-Aufbau occupation as described in the text.

The AILFT analysis suggests that in both **FeCl** and **FeCH$_3$** the d_{yz} orbital is lowest in energy. However, the lowest state is shown to have a dominant configuration (~90%) where the z^2 orbital is doubly occupied (Figures 9 and 10 (left)). This non-Aufbau ground state indicates that there is a strong competition between electron repulsion and the ligand field, where the energy of the ground state is minimized when the lowest one-electron AILFT orbital remains singly occupied and the second lowest orbital is doubly occupied such that the lowest energy configuration is $\left[d^1_{yz} d^2_{z^2} d^1_{xz} d^1_{x^2-y^2} d^1_{xy} \right]$. This is the same orbital occupancy proposed previously by Andres et al.,[4] but their analysis did not reveal the non-Aufbau occupation pattern so that their Aufbau occupancy, as shown in Figure 1, is $\left[d^2_{z^2} d^1_{yz} d^1_{xz} d^1_{x^2-y^2} d^1_{xy} \right]$.

After the inclusion of spin orbit coupling, the calculations for both **FeCl** and **FeCH$_3$** predict negative axial values of the zero-field parameter, D, and with $|E/D| = 0.04$ for both compounds. This is consistent with their X-band EPR spectra, namely that these showed low field (high g') transitions.[4] For **FeCl** the ground state quasi-doublet is calculated to be separated by ~0.27 cm^{-1} (i.e., in the X-band EPR energy range) with the first excited states at 138 and 151 cm^{-1}. The calculations on **FeCH$_3$** predict a nearly identical separation of the ground quasi-doublet (0.26 cm^{-1}) and first excited quasi-doublet at 135 and 148 cm^{-1}. These values are all reasonably close to the experimental values and reproduce the slightly larger energy transitions in the FIRMS results of **FeCl** compared to the **FeCH$_3$**. The origin of this large zfs is understood by examining the low-lying excited states and their interaction with the ground state via spin-orbit coupling (Figure 10). By far the largest contribution to zfs is the coupling between the nearly degenerate orbital pair (d_{yz} and d_{z^2}). This is consistent with the explanation previously given by Andres et al.[4]

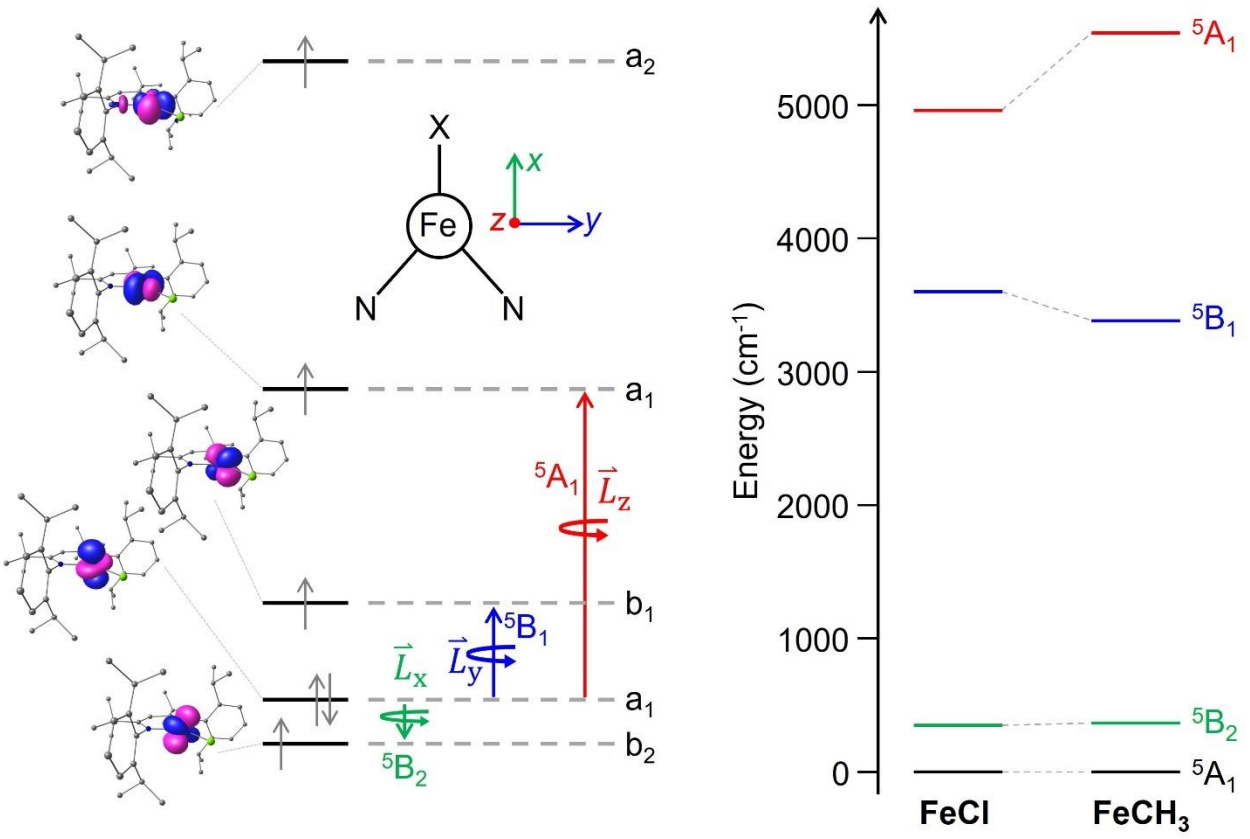

Figure 10. The left-hand side shows a qualitative orbital energy level diagram for **FeX** with the dominate, non-Aufbau, ground state configuration shown. The inset shows the axis definition which has been chosen to be consistent with previous studies of these compounds (see also Figure 1). The transitions and associated excited states are colored to indicate the orbital angular momentum operator responsible for their interaction with the ground state (red, $\hat{L}_z$; blue, $\hat{L}_y$; green, $\hat{L}_x$). The diagram on the right shows the relative energies of the low-lying excited states, color coded as on the left.

As seen in Figure 9, the AILFT orbital level diagram predicts the same qualitative ordering of the *d*-orbitals in **CoCl** and **CoCH$_3$** as their Fe analogues. Interestingly, in both **CoX** complexes the CASSCF-AILFT derived ground state contains two major configurations $\left[d_{z^2}^1 d_{yz}^2 d_{xz}^1 d_{x^2-y^2}^2 d_{xy}^1 \right]$ (55% in **CoCl**, 45% **CoCH$_3$**) and $\left[d_{z^2}^2 d_{yz}^2 d_{xz}^1 d_{x^2-y^2}^1 d_{xy}^1 \right]$ (42% in both **CoCl** and **CoCH$_3$**). The experimentally determined and CASSCF/NEVPT2 calculated (in parenthesis) g'-values of **CoCl** are g_x' = 5.64 (6.12), g_y' = 4.62 (4.94), and g_z' = 1.97 (1.92). These values are consistent with a positive value of D, where the calculated value of D = +65.5 cm^{-1} ($|E/D|$ = 0.07 – in good agreement with the experimental value from

X-band EPR of **CoCl**) corresponding to a zero-field gap of $2D^* = 132$ cm^{-1}, a slight overestimation of the experimental value. As discussed above, the X-band EPR spectrum of **CoCH$_3$** shows only a single observable g'-value, $g_z'_{(max)} = 8.50$, which suggests this compound displays a negative D. The CASSCF/NEVPT2 calculations result in $g_z' = 9.94$, $D = -122.5$ cm^{-1}, $|E/D| = 0.04$ that corresponds to a zero-field gap of 245 cm^{-1}. The difference in the sign of D between **CoCl** and **CoCH$_3$** can be rationalized by examining how the excited states couple through the spin-orbit interaction into the ground state. This is shown in Figure 11 (right), which reveals that there is a substantial reordering of the excited state energies between the two compounds. This energetic reordering is responsible for the change in the sign of D and can be explained qualitatively by the difference between the methyl and chlorido ligands. The increase in energy of both the $^4B_1$ and, more importantly, $^4A_2$ excited states upon going from **CoCH$_3$** to **CoCl** (Figure 11, right; also Figure 9) arises from the increase in energy of the b_1 (d_{xz}) and a_2 (d_{xy}) orbitals as result of adding π-donation from Cl^- (along x) that is absent in the σ-only donor CH_3^-. There is a counteracting decrease in energy of the $^4A_1$ excited state upon going from **CoCH$_3$** to **CoCl** caused by the a_1 ($d_{x^2-y^2}$) orbital decreasing in energy as the stronger σ-donor methyl is replaced by chloride. But this reordering has a lesser effect on the zfs as $^4A_1$ is more weakly coupled to the $^4B_2$ ground state than either $^4B_1$ and $^4A_2$ are. Additionally, Table S6 lists the major SOC contributions from excited states to the zfs of **CoX**.

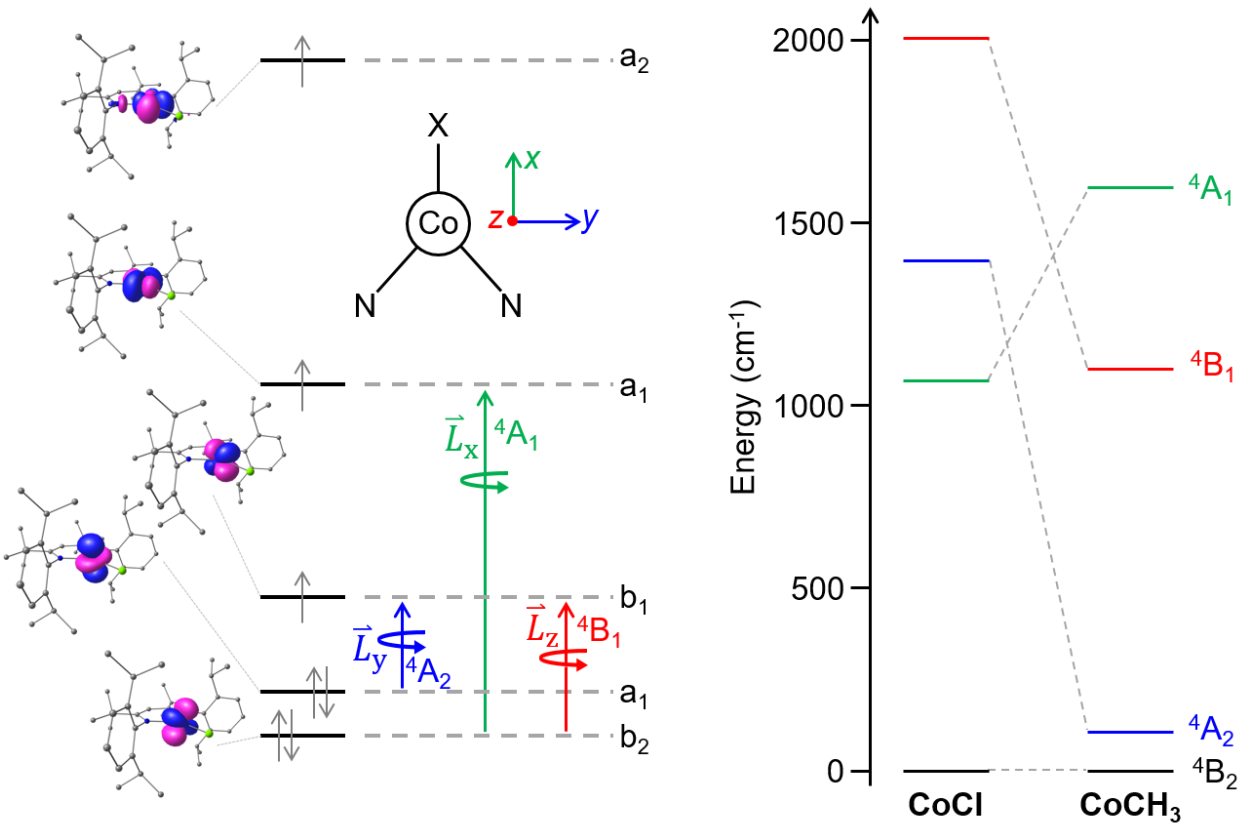

Figure 11. The left-hand side shows a qualitative orbital energy level diagram for **CoX** with the dominate ground state configuration shown. The inset defines the choice of axis which has been chosen to be consistent with previous studies of the Fe analogues of these compounds (see also Figure 1). The transitions and associated excited states are colored to indicate the orbital angular momentum operator responsible for their interaction with the ground state (red, $\hat{L}_z$; blue, $\hat{L}_y$; green, $\hat{L}_x$). The diagram on the right shows the energies of the low-lying excited states for **CoCl** and **CoCH$_3$**, color coded as on the left, and the reorganization of these states that is responsible for the change in the sign of D between **CoCl** and **CoCH$_3$**.

The AILFT values for ζ, B, and C can be input into the LFT software (DDN program) along with the single electron d orbital energies (Table 2) to yield spin Hamiltonian parameters for modelling **MX** as a pure d^n system. For the **FeX** complexes, this demonstrates that there is a single g' that is large, consistent with experiment. Use of an applied field of 50 mT (corresponding roughly to the experimental X-band resonant field) gives $g' \approx 11.3(1)$ for both **FeCl** and **FeCH$_3$**, in good agreement with the observed values (10.9 for **FeCl** and 11.4 for **FeCH$_3$**).[4] Moreover, the direction is correct in that this is g' along x – the Fe-X bond. The splitting of the ground state quintet gives -50 cm$^{-1} > D > -70$ cm^{-1} for both **FeX** complexes, the negative sign and large magnitude as seen experimentally. In the case of **CoCl**, this procedure gives a splitting $2D^* \approx 170$ cm^{-1}. Ignoring the rhombic splitting, which cannot be extracted from this calculation and is in any case small, gives $D \approx +85$ cm^{-1}, ~50% off from experiment (Table 1). The sign can be readily determined since the lower doublet has spin magnitude ±0.31 and is thus $m_S = \pm 1/2$, while the higher doublet has spin magnitude ±1.19 and is $m_S = \pm 3/2$. These values were calculated using an applied field $B_0 = 300$ mT – a typical X-band resonant field. This calculation also yielded $\mathbf{g}' = [2.38, 8.55, 1.32]$ (given as g_x, g_y, g_z, rather than the observed g_{max}, g_{mid}, g_{min}). This $\mathbf{g}'$ is quite different from that observed for **CoCl**, and requires a rather peculiar set of intrinsic parameters: $E/D = 1/3$ with $\mathbf{g} = [2.38, 3.13, 1.80]$. For **CoCH$_3$**, the spin magnitudes are more ambiguous (lower doublet ±0.06; higher doublet ±0.44), but the higher spin doublet clearly corresponds to $m_S = \pm 1/2$, hence the negative sign given here for D. The calculated $2D^* \approx 278$ cm^{-1}, so $D \approx -139$ cm^{-1}, larger magnitude that what is found experimentally, and $\mathbf{g}' = [0.36, 10.08, 0.24]$ (again as g_x, g_y, g_z, rather than the observed g_{max}, g_{mid}, g_{min}), which is consistent with the limited experimental information. Overall, AILFT reproduces well the low-field X-band EPR resonances observed for both **FeX** and **CoCH$_3$**, although not the "conventional" EPR signature of **CoCl**, with the **g** anisotropy and zfs of both **CoX** complexes being overstated.

QCT Calculated Mössbauer Parameters and ^{57}Fe, ^{59}Co, and ^{14}N Hyperfine Couplings. Thanks to the use of variable applied magnetic fields, along with the standard Mössbauer parameters, namely isomer shift, δ, and quadrupole splitting ΔE_Q, the study by Andres et al. reported an internal magnetic field, $\boldsymbol{B}_{int}$, along the x axis (i.e., C_2 axis, see Figure 1) that was quite large, +62 T for **FeCl** and +82 T for **FeCH$_3$**.[4] Subsequently, in a study of N_2-binding involving related Fe^{II} and Fe^{I} β-diketiminate complexes,[121] DFT calculations were performed on **FeCl** and **FeCH$_3$** as well as on the novel complexes in that work. The relevant results are summarized in Table S5. This was a pioneering study given the state

of DFT calculations at that time and Stoian et al. were able to reproduce the δ and ΔE_Q values reasonably well, even given the near orbital degeneracy of the **FeX** system. Indeed, we obtain essentially the same results for these parameters, despite using more highly developed software and having the benefit of extensive computational benchmarking of ^{57}Fe Mössbauer data.[79, 122] We note that although ab initio (CASSCF) methods are suitable for the purely electronic parameters (i.e., zfs as well as orbital energies), the use of DFT for nuclear-electronic parameters (i.e., hyperfine coupling) we believe is still the optimal approach.[123-126] The calculated quadrupole splitting is reasonably close to experiment (see Table S5) although the calculated asymmetry parameter ($\eta = V_{\text{mid}} - V_{\text{min}})/V_{\text{max}}$) is not, being too high for **FeCl** and too low for **FeCH$_3$**. In D_{3h} (or C_{3h}) symmetry as in the idealized complex in Figure 1 (left), $\eta = 0$, so the results here demonstrate the difficulty in quantifying the in-plane bonding (electron distribution) in **FeX** albeit not the out-of-plane behavior. The situation with respect to hyperfine coupling is more complicated as this depends on the difference between α and β spin densities at the nucleus as opposed to their sum, which determines the isomer shift. As noted above, the complete **A**(^{57}Fe) tensor was not determined for **FeX**, only the component along the Fe-X bond. We find here that the largest magnitude calculated component is quite far off from experiment (see Table S5) indicating the challenge of such calculations even with current computational power. Lacking the extreme orbital near-degeneracy of the **FeX** complexes, the **CoX** complexes present a potentially more fruitful area for hyperfine coupling calculations. In principle, the quadrupole coupling (i.e., yielding the electric field gradient, V_{ii}) of ^{59}Co could also be determined from EPR/ENDOR, as is possible for (excited state) ^{57}Fe from Mössbauer, but this was not possible and rarely is, although it has been determined for ^{51}V in vanadyl complexes.[127] We also observe only one component of the hyperfine coupling in **CoCH$_3$**. The calculated **A**(^{59}Co) for **CoCl** appears to underestimate the overall coupling as well as being much more anisotropic than observed. We have no explanation for this discrepancy other than the difficulty in quantifying the small difference between α and β spin populations, which affected the **FeX** calculations as well. Despite this, the calculated **A**(^{14}N) for the nacnac ligands in **CoCl** agrees reasonably well with experiment (Table S5), with A_{iso}(^{14}N) differing by only ~1 MHz (~15 – 20%). The calculation also supports the two ^{14}N being essentially magnetically equivalent. The calculated ^{14}N quadrupole coupling for **CoCl** also matches experiment with each component agreeing within ~0.1 MHz (Table S5).

Conclusions

The β-diketiminate (nacnac) ligand is widely used in coordination chemistry and can support complexes with low coordination numbers. The electronic structure of four pairwise related nacnac-supported three-coordinate complexes, two each of Fe^{II} and Co^{II} and two each with chlorido and methyl ancillary ligands, is examined in detail here. The two iron(II) complexes had been previously studied by applied-field Mössbauer spectroscopy,[4] but QCT calculations of the type performed here were impossible 20 years ago. The zfs in these Fe^{II} complexes was inferred earlier only from the Mössbauer measurements. Here we directly observe their zfs thanks to the use of far-infrared magnetic spectroscopy (FIRMS). These measurements definitively show the large magnitude negative zfs in both **FeCl** and **FeCH$_3$** (respectively, D = –38 and –37 cm^{-1}), with very low rhombicity ($|E/D|$ = 0.05 and 0.03, respectively). It is notable that despite the differences between a methyl and chlorido ligand, the zfs is essentially the same in the two **FeX** complexes. This finding has implications for the design of SMMs in that the overall geometry rather than the identities of the coordinating ligands may be the key factor, at least in S = 2 systems. In the case of the two cobalt(II) complexes, no theoretical analysis of electronic structure or advanced spectroscopic measurements had been previously performed. In these Kramers (half-integer spin) ions, conventional EPR and ENDOR spectroscopy provided information on metal (via ^{59}Co hyperfine coupling from EPR) and ligand (via ^{14}N hyperfine coupling from ENDOR) spin delocalization. The results for both metal and ligand are consistent with those for related Co^{II} complexes, and the present study provided the first measurement of a ^{14}N hyperfine coupling for a β-diketiminate complex. The **CoX** complexes exhibit large magnitude zfs (respectively, D = +55 and –49 cm^{-1}), but with a sign change from positive in **CoCl** to negative in **CoCH$_3$** that comes from a rearrangement of excited-state energies due to the donor properties of Cl^- versus CH_3^-. Thus, the nature of the third donor may be crucial in determining the details of electronic structure in S = 3/2 systems. Calculation of spectroscopic parameters obtained from Mössbauer and EPR spectroscopy in its various forms still represents a challenge even using *ab initio* methods – at least for the low-coordinate **MX** systems studied here. We hope that theoreticians will take up this challenge so that a better understanding of the origin of the parameters can be obtained, which will assist in the design of such complexes with desired magnetic properties.

Notes

The authors declare no competing financial interests.

Acknowledgements

We thank the National Institutes of Health for funding (GM-065313 to P. L. H.; F32-GM136179 to M. S. F.) Part of this work was performed at the National High Magnetic Field Laboratory which is supported by NSF Cooperative Agreement No. DMR-1644779 and the State of Florida. We thank Prof. Brian M. Hoffman (Northwestern University) for use of X- and Q-band EPR (ENDOR) spectrometers, which are supported by funding from the U. S. Department of Energy (DOE) Office of Science, Basic Energy Sciences (BES) under contract DE-SC0019342 (to B. M. H.) and the NSF (grant MCB-1908587 to B. M. H.). Part of this work was supported by the Laboratory Directed Research and Development (LDRD) program at Los Alamos National Laboratory (20230399ER). We also thank Dr. Hao Yang, Northwestern University, for assistance with the pulsed ENDOR measurements and Profs. David L. Tierney, Miami University, and Sebastian A. Stoian, University of Idaho, for helpful comments. We thank Prof. Jesper Bendix (Copenhagen U., Denmark) for the LFT program Ligfield.

Supporting Information

Additional EPR, ENDOR, and FIRMS spectra. Tables of LFT fits and QCT results. This material is available free of charge at http://pubs.acs.org/.

Present addresses:

A. L. Nagelski: Chemistry Division, Los Alamos National Laboratory, Los Alamos, New Mexico 87545, United States

M. S. Fataftah: Department of Chemistry, University of Illinois at Urbana-Champaign, Urbana, Illinois 61801, United States

References

1. Alvarez, S., Bonding and stereochemistry of three-coordinated transition metal compounds. *Coord. Chem. Rev.* **1999,** *193-195*, 13-41.
2. Panda, A.; Stender, M.; Wright, R. J.; Olmstead, M. M.; Klavins, P.; Power, P. P., Synthesis and Characterization of Three-Coordinate and Related β-Diketiminate Derivatives of Manganese, Iron, and Cobalt. *Inorg. Chem.* **2002,** *41*, 3909-3916.
3. Sanakis, Y.; Power, P. P.; Stubna, A.; Münck, E., Mössbauer Study of the Three-Coordinate Planar FeII Thiolate Complex $[Fe(SR)_3]^-$ (R = C_6H_2-2,4,6-*t*Bu_3): Model for the Trigonal Iron Sites of the $MoFe_7S_9$:Homocitrate Cofactor of Nitrogenase. *Inorg. Chem.* **2002,** *41*, 2690-2696.
4. Andres, H.; Bominaar, E. L.; Smith, J. M.; Eckert, N. A.; Holland, P. L.; Münck, E., Planar Three-Coordinate High-Spin Fe^{II} Complexes with Large Orbital Angular Momentum: Mössbauer, Electron Paramagnetic Resonance, and Electronic Structure Studies. *J. Am. Chem. Soc.* **2002,** *124*, 3012-3025.
5. Holland, P. L.; Cundari, T. R.; Perez, L. L.; Eckert, N. A.; Lachicotte, R. J., Electronically Unsaturated Three-Coordinate Chloride and Methyl Complexes of Iron, Cobalt, and Nickel [J. Am. Chem. Soc. 2002, 124 (48), 14416−14424]. *J. Am. Chem. Soc.* **2003,** *125*, 11772-11772.
6. Dai, X.; Warren, T. H., Discrete Bridging and Terminal Copper Carbenes in Copper-Catalyzed Cyclopropanation. *J. Am. Chem. Soc.* **2004,** *126*, 10085-10094.
7. Melzer, M. M.; Jarchow-Choy, S.; Kogut, E.; Warren, T. H., Reductive Cleavage of O-, S-, and N-Organonitroso Compounds by Nickel(I) β-Diketiminates. *Inorg. Chem.* **2008,** *47*, 10187-10189.
8. Rose, R. P.; Jones, C.; Schulten, C.; Aldridge, S.; Stasch, A., Synthesis and Characterization of Amidinate–Iron(I) Complexes: Analogies with β-Diketiminate Chemistry. *Chem. Eur. J.* **2008,** *14*, 8477-8480.
9. Power, P. P., Stable Two-Coordinate, Open-Shell (d^1–d^9) Transition Metal Complexes. *Chem. Rev.* **2012,** *112*, 3482-3507.
10. Chandrasekaran, P.; Chiang, K. P.; Nordlund, D.; Bergmann, U.; Holland, P. L.; DeBeer, S., Sensitivity of X-ray Core Spectroscopy to Changes in Metal Ligation: A Systematic Study of Low-Coordinate, High-Spin Ferrous Complexes. *Inorg. Chem.* **2013,** *52*, 6286-6298.
11. Danopoulos, A. A.; Braunstein, P.; Wesolek, M.; Monakhov, K. Y.; Rabu, P.; Robert, V., Three-Coordinate Iron(II) N-Heterocyclic Carbene Alkyl Complexes. *Organometallics* **2012,** *31*, 4102-4105.
12. Davis, T. L.; Watts, J. L.; Brown, K. J.; Hewage, J. S.; Treleven, A. R.; Lindeman, S. V.; Gardinier, J. R., Structural classification of metal complexes with three-coordinate centres. *Dalton Trans.* **2015,** *44*, 15408-15412.

13. Pratt, J.; Bryan, A. M.; Faust, M.; Boynton, J. N.; Vasko, P.; Rekken, B. D.; Mansikkamäki, A.; Fettinger, J. C.; Tuononen, H. M.; Power, P. P., Effects of Remote Ligand Substituents on the Structures, Spectroscopic, and Magnetic Properties of Two-Coordinate Transition-Metal Thiolate Complexes. *Inorg. Chem.* **2018,** *57*, 6491-6502.
14. Rau, I. G.; Baumann, S.; Rusponi, S.; Donati, F.; Stepanow, S.; Gragnaniello, L.; Dreiser, J.; Piamonteze, C.; Nolting, F.; Gangopadhyay, S.; Albertini, O. R.; Macfarlane, R. M.; Lutz, C. P.; Jones, B. A.; Gambardella, P.; Heinrich, A. J.; Brune, H., Reaching the magnetic anisotropy limit of a 3d metal atom. *Science* **2014,** *344*, 988-992.
15. Layfield, R. A., Organometallic Single-Molecule Magnets. *Organometallics* **2014,** *33*, 1084-1099.
16. Gómez-Coca, S.; Aravena, D.; Morales, R.; Ruiz, E., Large magnetic anisotropy in mononuclear metal complexes. *Coord. Chem. Rev.* **2015,** *289-290*, 379-392.
17. Deng, Y.-F.; Han, T.; Yin, B.; Zheng, Y.-Z., On balancing the QTM and the direct relaxation processes in single-ion magnets – the importance of symmetry control. *Inorg. Chem. Front.* **2017,** *4*, 1141-1148.
18. Reiff, W. M.; LaPointe, A. M.; Witten, E. H., Virtual Free Ion Magnetism and the Absence of Jahn−Teller Distortion in a Linear Two-Coordinate Complex of High-Spin Iron(II). *J. Am. Chem. Soc.* **2004,** *126*, 10206-10207.
19. Reiff, W. M.; Schulz, C. E.; Whangbo, M.-H.; Seo, J. I.; Lee, Y. S.; Potratz, G. R.; Spicer, C. W.; Girolami, G. S., Consequences of a Linear Two-Coordinate Geometry for the Orbital Magnetism and Jahn−Teller Distortion Behavior of the High Spin Iron(II) Complex Fe[N(*t*-Bu)$_2$]$_2$. *J. Am. Chem. Soc.* **2009,** *131*, 404-405.
20. Merrill, W. A.; Stich, T. A.; Brynda, M.; Yeagle, G. J.; Fettinger, J. C.; Hont, R. D.; Reiff, W. M.; Schulz, C. E.; Britt, R. D.; Power, P. P., Direct Spectroscopic Observation of Large Quenching of First-Order Orbital Angular Momentum with Bending in Monomeric, Two-Coordinate Fe(II) Primary Amido Complexes and the Profound Magnetic Effects of the Absence of Jahn− and Renner−Teller Distortions in Rigorously Linear Coordination. *J. Am. Chem. Soc.* **2009,** *131*, 12693-12702.
21. Freedman, D. E.; Harman, W. H.; Harris, T. D.; Long, G. J.; Chang, C. J.; Long, J. R., Slow Magnetic Relaxation in a High-Spin Iron(II) Complex. *J. Am. Chem. Soc.* **2010,** *132*, 1224-1225.
22. Lin, P.-H.; Smythe, N. C.; Gorelsky, S. I.; Maguire, S.; Henson, N. J.; Korobkov, I.; Scott, B. L.; Gordon, J. C.; Baker, R. T.; Murugesu, M., Importance of Out-of-State Spin–Orbit Coupling for Slow Magnetic Relaxation in Mononuclear Fe^{II} Complexes. *J. Am. Chem. Soc.* **2011,** *133*, 15806-15809.
23. Bryan, A. M.; Merrill, W. A.; Reiff, W. M.; Fettinger, J. C.; Power, P. P., Synthesis, Structural, and Magnetic Characterization of Linear and Bent Geometry Cobalt(II) and Nickel(II) Amido Complexes: Evidence of Very Large Spin–Orbit Coupling Effects in Rigorously Linear Coordinated Co^{2+}. *Inorg. Chem.* **2012,** *51*, 3366-3373.

24. Zadrozny, J. M.; Atanasov, M.; Bryan, A. M.; Lin, C.-Y.; Rekken, B. D.; Power, P. P.; Neese, F.; Long, J. R., Slow magnetization dynamics in a series of two-coordinate iron(II) complexes. *Chem. Sci.* **2013,** *4*, 125-138.
25. Atanasov, M.; Zadrozny, J. M.; Long, J. R.; Neese, F., A theoretical analysis of chemical bonding, vibronic coupling, and magnetic anisotropy in linear iron(II) complexes with single-molecule magnet behavior. *Chem. Sci.* **2013,** *4*, 139-156.
26. Zadrozny, J. M.; Xiao, D. J.; Atanasov, M.; Long, G. J.; Grandjean, F.; Neese, F.; Long, J. R., Magnetic blocking in a linear iron(I) complex. *Nat Chem* **2013,** *5*, 577-581.
27. Zadrozny, J. M.; Xiao, D. J.; Long, J. R.; Atanasov, M.; Neese, F.; Grandjean, F.; Long, G. J., Mössbauer Spectroscopy as a Probe of Magnetization Dynamics in the Linear Iron(I) and Iron(II) Complexes $[Fe(C(SiMe_3)_3)_2]^{1-/0}$. *Inorg. Chem.* **2013,** *52*, 13123-13131.
28. Samuel, P. P.; Mondal, K. C.; Amin Sk, N.; Roesky, H. W.; Carl, E.; Neufeld, R.; Stalke, D.; Demeshko, S.; Meyer, F.; Ungur, L.; Chibotaru, L. F.; Christian, J.; Ramachandran, V.; van Tol, J.; Dalal, N. S., Electronic Structure and Slow Magnetic Relaxation of Low-Coordinate Cyclic Alkyl(amino) Carbene Stabilized Iron(I) Complexes. *J. Am. Chem. Soc.* **2014,** *136*, 11964-11971.
29. Bryan, A. M.; Long, G. J.; Grandjean, F.; Power, P. P., Synthesis, Structural, Spectroscopic, and Magnetic Characterization of Two-Coordinate Cobalt(II) Aryloxides with Bent or Linear Coordination. *Inorg. Chem.* **2014,** *53*, 2692-2698.
30. Eichhöfer, A.; Lan, Y.; Mereacre, V.; Bodenstein, T.; Weigend, F., Slow Magnetic Relaxation in Trigonal-Planar Mononuclear Fe(II) and Co(II) Bis(trimethylsilyl)amido Complexes—A Comparative Study. *Inorg. Chem.* **2014,** *53*, 1962-1974.
31. Schulte, K. A.; Vignesh, K. R.; Dunbar, K. R., Effects of coordination sphere on unusually large zero field splitting and slow magnetic relaxation in trigonally symmetric molecules. *Chem. Sci.* **2018,** *9*, 9018-9026.
32. Bunting, P. C.; Atanasov, M.; Damgaard-Møller, E.; Perfetti, M.; Crassee, I.; Orlita, M.; Overgaard, J.; van Slageren, J.; Neese, F.; Long, J. R., A linear cobalt(II) complex with maximal orbital angular momentum from a non-Aufbau ground state. *Science* **2018,** *362*, eaat7319.
33. Thomsen, M. K.; Nyvang, A.; Walsh, J. P. S.; Bunting, P. C.; Long, J. R.; Neese, F.; Atanasov, M.; Genoni, A.; Overgaard, J., Insights into Single-Molecule-Magnet Behavior from the Experimental Electron Density of Linear Two-Coordinate Iron Complexes. *Inorg. Chem.* **2019,** *58*, 3211-3218.
34. Sarkar, A.; Dey, S.; Rajaraman, G., Role of Coordination Number and Geometry in Controlling the Magnetic Anisotropy in Fe^{II}, Co^{II}, and Ni^{II} Single-Ion Magnets. *Chem. Eur. J.* **2020,** *26*, 14036-14058.
35. Saber, M. R.; Przyojski, J. A.; Tonzetich, Z. J.; Dunbar, K. R., Slow magnetic relaxation in cobalt N-heterocyclic carbene complexes. *Dalton Trans.* **2020,** *49*, 11577-11582.

36. Jung, J.; Legendre, C. M.; Demeshko, S.; Herbst-Irmer, R.; Stalke, D., Trigonal Planar Iron(II) and Cobalt(II) Complexes Containing [RS(N*t*Bu)3]n− (R = N*t*Bu, n = 2; CH_2PPh_2, *n* = 1) as Acute Bite-Angle Chelating Ligands: Soft P Donor Proves Beneficial to Magnetic Co Species. *Inorg. Chem.* **2021,** *60*, 9580-9588.
37. Blackaby, W. J. M.; Harriman, K. L. M.; Greer, S. M.; Folli, A.; Hill, S.; Krewald, V.; Mahon, M. F.; Murphy, D. M.; Murugesu, M.; Richards, E.; Suturina, E.; Whittlesey, M. K., Extreme g-Tensor Anisotropy and Its Insensitivity to Structural Distortions in a Family of Linear Two-Coordinate Ni(I) Bis-N-heterocyclic Carbene Complexes. *Inorg. Chem.* **2022,** *61*, 1308-1315.
38. Münster, K.; Baabe, D.; Kintzel, B.; Böhme, M.; Plass, W.; Raeder, J.; Walter, M. D., Low-Coordinate Iron(II) Amido Half-Sandwich Complexes with Large Internal Magnetic Hyperfine Fields. *Inorg. Chem.* **2022,** *61*, 18883-18898.
39. Khurana, R.; Ali, M. E., Single-Molecule Magnetism in Linear Fe(I) Complexes with Aufbau and Non-Aufbau Ground States. *Inorg. Chem.* **2022,** *61*, 15335-15345.
40. Gatteschi, D.; Sessoli, R., Quantum Tunneling of Magnetization and Related Phenomena in Molecular Materials. *Angew. Chem. Int. Ed.* **2003,** *42*, 268-297.
41. Waldmann, O., A Criterion for the Anisotropy Barrier in Single-Molecule Magnets. *Inorg. Chem.* **2007,** *46*, 10035-10037.
42. Zadrozny, J. M.; Liu, J.; Piro, N. A.; Chang, C. J.; Hill, S.; Long, J. R., Slow magnetic relaxation in a pseudotetrahedral cobalt(II) complex with easy-plane anisotropy. *Chem. Commun.* **2012,** *48*, 3927-3929.
43. Bourget-Merle, L.; Lappert, M. F.; Severn, J. R., The Chemistry of β-Diketiminatometal Complexes. *Chem. Rev.* **2002,** *102*, 3031-3066.
44. Mindiola, D. J.; Holland, P. L.; Warren, T. H., Complexes of Bulky β-Diketiminate Ligands. In *Inorg. Synth.*, 2010; pp 1-55.
45. Chen, C.; Bellows, S. M.; Holland, P. L., Tuning steric and electronic effects in transition-metal β-diketiminate complexes. *Dalton Trans.* **2015,** *44*, 16654-16670.
46. Webster, R. L., β-Diketiminate complexes of the first row transition metals: applications in catalysis. *Dalton Trans.* **2017,** *46*, 4483-4498.
47. We shall employ the nomenclature nacnac$^{R,R'}$ wherein R = the N-substituent and R′ = the "backbone" aliphatic group, e.g., Me for the simplest ligand, 2,4-bis([R]imido)-3-pentyl anion, and *t*Bu for that used herein, 2,2,6,6-tetramethyl-3,5-bis([R]imido)-4-heptyl anion.
48. Arslan, E.; Lalancette, R. A.; Bernal, I., An historic and scientific study of the properties of metal(III) tris-acetylacetonates. *Structural Chemistry* **2017,** *28*, 201-212.
49. Latreche, S.; Schaper, F., Chromium(III) Bis(diketiminate) Complexes. *Organometallics* **2010,** *29*, 2180-2185.
50. Lazarov, B. B.; Hampel, F.; Hultzsch, K. C., Synthesis and Structural Characterization of β-Diketiminato Yttrium Complexes and their Application in Epoxide/CO_2-Copolymerization. *Z. Anorg. Allg. Chem.* **2007,** *633*, 2367-2373.

51. C. Andrews, P.; L. Atwood, J.; J. Barbour, L.; D. Croucher, P.; J. Nichols, P.; O. Smith, N.; W. Skelton, B.; H. White, A.; L. Raston, C., Supramolecular confinement of C_{60}, S_8, P_4Se_3 and toluene by metal(II) macrocyclic complexes. *J. Chem. Soc., Dalton Trans.* **1999**, 2927-2932.
52. Kumar Sahu, P.; Kharel, R.; Shome, S.; Goswami, S.; Konar, S., Understanding the unceasing evolution of Co(II) based single-ion magnets. *Coord. Chem. Rev.* **2023,** *475*, 214871.
53. Smith, J. M.; Lachicotte, R. J.; Holland, P. L., Tuning metal coordination number by ancillary ligand steric effects: synthesis of a three-coordinate iron(II)complex. *Chem. Commun.* **2001**, 1542-1543.
54. Holland, P. L.; Cundari, T. R.; Perez, L. L.; Eckert, N. A.; Lachicotte, R. J., Electronically Unsaturated Three-Coordinate Chloride and Methyl Complexes of Iron, Cobalt, and Nickel. *J. Am. Chem. Soc.* **2002,** *124*, 14416-14424.
55. Brackett, G. C.; Richards, P. L.; Caughey, W. S., Far-infrared magnetic resonance in Fe(III) and Mn(III) porphyrins, myoglobin, hemoglobin, ferrichrome A, and Fe(III) dithiocarbamates. *J. Chem. Phys.* **1971,** *54*, 4383-4401.
56. Champion, P. M.; Sievers, A. J., Far infrared magnetic resonance in $FeSiF_6{\cdot}6H_2O$ and $Fe(SPh)_4^{2-}$. *J. Chem. Phys.* **1977,** *66*, 1819-1825.
57. Chiang, K. P.; Barrett, P. M.; Ding, F.; Smith, J. M.; Kingsley, S.; Brennessel, W. W.; Clark, M. M.; Lachicotte, R. J.; Holland, P. L., Ligand Dependence of Binding to Three-Coordinate Fe(II) Complexes. *Inorg. Chem.* **2009,** *48*, 5106-5116.
58. Werst, M. M.; Davoust, C. E.; Hoffman, B. M., Ligand Spin Densities in Blue Copper Proteins by Q-band ^1H and ^{14}N ENDOR Spectroscopy. *J. Am. Chem. Soc.* **1991,** *113*, 1533-1538.
59. Davoust, C. E.; Doan, P. E.; Hoffman, B. M., Q-Band Pulsed Electron Spin-Echo Spectrometer and Its Application to ENDOR and ESEEM. *J. Magn. Reson., Ser. A* **1996,** *119*, 38-44.
60. Davies, E. R., A New Pulse ENDOR Technique. *Physics Letters A* **1974,** *47*, 1-2.
61. Mailer, C.; Hoffman, B. M., Tumbling of an adsorbed nitroxide using rapid adiabatic passage. *J. Phys. Chem.* **1976,** *80*, 842-846.
62. Mailer, C.; Taylor, C. P. S., Rapid adiabatic passage EPR of ferricytochrome c. Signal enhancement and determination of the spin-lattice relaxation time. *Biochimica et Biophysica Acta* **1973,** *322*, 195-203.
63. Belford, R. L.; Nilges, M. J. In *Computer Simulations of Powder Spectra*, EPR Symposium, 21st Rocky Mountain Conference, Denver, Colorado, Denver, Colorado, August,1979.
64. Belford, R. L.; Belford, G. G., Eigenfield expansion technique for efficient computation of field-swept fixed-frequency spectra from relaxation master equations. *J. Chem. Phys.* **1973,** *59*, 853-854.

65. Bain, G. A.; Berry, J. F., Diamagnetic Corrections and Pascal's Constants. *J. Chem. Educ.* **2008,** *85*, 532-536.
66. Azuah, R. T.; Kneller, L. R.; Qiu, Y.; Tregenna-Piggott, P. L. W.; Brown, C. M.; Copley, J. R. D.; Dimeo, R. M., DAVE: A Comprehensive Software Suite for the Reduction, Visualization, and Analysis of Low Energy Neutron Spectroscopic Data. *Journal of Research of the National Institute of Standards and Technology* **2009,** *114*, 341-358.
67. Nehrkorn, J.; Telser, J.; Holldack, K.; Stoll, S.; Schnegg, A., Simulating Frequency-Domain Electron Paramagnetic Resonance: Bridging the Gap between Experiment and Magnetic Parameters for High-Spin Transition-Metal Ion Complexes. *J. Phys. Chem. B* **2015,** *119*, 13816-13824.
68. Stoll, S. EasySpin. http://www.easyspin.org/.
69. Abragam, A.; Bleaney, B., *Electron Paramagnetic Resonance of Transition Ions (Oxford Classic Texts in the Physical Sciences)*. Oxford University Press: Oxford, UK, 2012.
70. Bendix, J., Ligfield. In *Comprehensive Coordination Chemistry II, Volume 2: Fundamentals: Physical Methods, Theoretical Analysis, and Case Studies*, Lever, A. B. P., Ed. Elsevier: Amsterdam, 2003; Vol. 2, pp 673-676.
71. Schönherr, T.; Atanasov, M.; Adamsky, H., Angular Overlap Model. In *Comprehensive Coordination Chemistry II*, McCleverty, J. A.; Meyer, T. J., Eds. Pergamon: Oxford, 2003; pp 443-455.
72. Schäffer, C. E.; Yamatera, H., Ligand field of conjugated bidentate ligands parametrized by the angular overlap model. *Inorg. Chem.* **1991,** *30*, 2840-2853.
73. Miessler, G. L.; Fischer, P. J.; Tarr, D. A., *Inorganic Chemistry*. Pearson: Upper Saddle River, NJ, 2014.
74. Neese, F., Software update: the ORCA program system, version 4.0. *Wiley Interdisciplinary Reviews: Computational Molecular Science* **2018,** *8*, e1327.
75. Perdew, J. P., Density-functional approximation for the correlation energy of the inhomogeneous electron gas. *Phys. Rev. B* **1986,** *33*, 8822-8824.
76. Perdew, J. P., Erratum: Density-functional approximation for the correlation energy of the inhomogeneous electron gas. *Phys. Rev. B* **1986,** *34*, 7406.
77. Becke, A. D., Density-functional exchange-energy approximation with correct asymptotic behavior. *Phys. Rev. A* **1988,** *38*, 3098-3100.
78. Weigend, F.; Ahlrichs, R., Balanced basis sets of split valence, triple zeta valence and quadruple zeta valence quality for H to Rn: Design and assessment of accuracy. *Phys. Chem. Chem. Phys.* **2005,** *7*, 3297-3305.
79. Römelt, M.; Ye, S.; Neese, F., Calibration of Modern Density Functional Theory Methods for the Prediction of ^{57}Fe Mössbauer Isomer Shifts: Meta-GGA and Double-Hybrid Functionals. *Inorg. Chem.* **2009,** *48*, 784-785.
80. Stoychev, G. L.; Auer, A. A.; Neese, F., Automatic Generation of Auxiliary Basis Sets. *J. Chem. Theory Comput.* **2017,** *13*, 554-562.

81. Hess, B. A., Relativistic electronic-structure calculations employing a two-component no-pair formalism with external-field projection operators. *Phys. Rev. A* **1986,** *33*, 3742-3748.
82. Angeli, C.; Bories, B.; Cavallini, A.; Cimiraglia, R., Third-order multireference perturbation theory: The n-electron valence state perturbation-theory approach. *J. Chem. Phys.* **2006,** *124*, 054108.
83. Xu, S.; Bucinsky, L.; Breza, M.; Krzystek, J.; Chen, C.-H.; Pink, M.; Telser, J.; Smith, J. M., Ligand Substituent Effects in Manganese Pyridinophane Complexes: Implications for Oxygen-Evolving Catalysis. *Inorg. Chem.* **2017,** *56*, 14315-14325.
84. A hypothetical MX_3 (e.g., X = Cl^-) would have D_{3h} symmetry, while C_{3h} retains all of the symmetry relevant to the present discussion and allows for inclusion of a hypothetical $M(XR)_3$ (e.g., XR = ^-OR, ^-SR) complex.
85. McNaughton, R. L.; Roemelt, M.; Chin, J. M.; Schrock, R. R.; Neese, F.; Hoffman, B. M., Experimental and Theoretical EPR Study of Jahn−Teller-Active [HIPTN$_3$N]MoL Complexes (L = N_2, CO, NH_3). *J. Am. Chem. Soc.* **2010,** *132*, 8645–8656.
86. Hendrich, M. P.; Debrunner, P. G., Integer-spin electron paramagnetic resonance of iron proteins. *Biophys. J.* **1989,** *56*, 489-506.
87. Surerus, K. K.; Hendrich, M. P.; Christie, P. D.; Rottgardt, D.; Orme-Johnson, W. H.; Münck, E., Moessbauer and integer-spin EPR of the oxidized P-clusters of nitrogenase: P^{OX} is a non-Kramers system with a nearly degenerate ground doublet. *J. Am. Chem. Soc.* **1992,** *114*, 8579-8590.
88. Münck, E.; Surerus, K. K.; Hendrich, M. P., Combining Mössbauer Spectroscopy with Integer Spin Electron Paramagnetic Resonance. *Methods in Enzymology* **1993,** *227*, 463-479.
89. Gupta, R.; Lacy, D. C.; Bominaar, E. L.; Borovik, A. S.; Hendrich, M. P., Electron Paramagnetic Resonance and Mössbauer Spectroscopy and Density Functional Theory Analysis of a High-Spin Fe^{IV}–Oxo Complex. *J. Am. Chem. Soc.* **2012,** *134*, 9775-9784.
90. Gupta, R.; Taguchi, T.; Borovik, A. S.; Hendrich, M. P., Characterization of Monomeric $Mn^{II/III/IV}$–Hydroxo Complexes from X- and Q-Band Dual Mode Electron Paramagnetic Resonance (EPR) Spectroscopy. *Inorg. Chem.* **2013,** *52*, 12568-12575.
91. Telser, J., EPR Interactions – Zero-Field Splittings. In *eMagRes*, John Wiley & Sons, Ltd: 2017; Vol. 6, pp 207-233.
92. Telser, J., Linewidth, field, and frequency in electron paramagnetic resonance (EPR) spectroscopy. *J. Biol. Inorg. Chem.* **2022,** *27*, 605-609.
93. Krzystek, J.; Ozarowski, A.; Telser, J., Multi-frequency, high-field EPR as a powerful tool to accurately determine zero-field splitting in high-spin transition metal coordination complexes. *Coord. Chem. Rev.* **2006,** *250*, 2308-2324.
94. Krzystek, J.; Telser, J., Measuring giant anisotropy in paramagnetic transition metal complexes with relevance to single-ion magnetism. *Dalton Trans.* **2016,** *45*, 16751-16763.

95. Banci, L.; Bencini, A.; Benelli, C.; Gatteschi, D.; Zanchini, C., Spectral-Structural Correlations in High-Spin Cobalt(II) Complexes. *Struct. Bonding* **1982,** *52*, 37-86.
96. Telser, J.; Drago, R. S., Correction: Reinvestigation of the Electronic and Magnetic Properties of Ruthenium Butyrate Chloride. *Inorg. Chem.* **1985,** *24*, 4765-4765.
97. Walsby, C. J.; Krepkiy, D.; Petering, D. H.; Hoffman, B. M., Cobalt-Substituted Zinc Finger 3 of Transcription Factor IIIA: Interactions with Cognate DNA Detected by ^{31}P ENDOR Spectroscopy. *J. Am. Chem. Soc.* **2003,** *125*, 7502-7503.
98. Makinen, M. W.; Kuo, L. C.; Yim, M. B.; Wells, G. B.; Fukuyama, J. M.; Kim, J. E., Ground term splitting of high-spin Co^{2+} as a probe of coordination structure. 1. Dependence of the splitting on coordination geometry. *J. Am. Chem. Soc.* **1985,** *107*, 5245-5255.
99. Baum, R. R.; Myers, W. K.; Greer, S. M.; Breece, R. M.; Tierney, D. L., The Original Co^{II} Heteroscorpionates Revisited: On the EPR of Pseudotetrahedral Co^{II}. *Eur. J. Inorg. Chem.* **2016,** *2016*, 2641-2647.
100. Converting from **g′** for Bp_2Co yields **g** = [2.35, 2.35, 2.03] with E/D = 0.004, so $A_z = A'_z$.
101. Van Doorslaer, S.; Jeschke, G.; Epel, B.; Goldfarb, D.; Eichel, R.-A.; Kräutler, B.; Schweiger, A., Axial solvent coordination in "base-off" Cob(II)alamin and related Co(II)-corrinates revealed by 2D-EPR. *J. Am. Chem. Soc.* **2003,** *125*, 5915-5927.
102. Przyojski, J. A.; Arman, H. D.; Tonzetich, Z. J., NHC Complexes of Cobalt(II) Relevant to Catalytic C–C Coupling Reactions. *Organometallics* **2013,** *32*, 723-732.
103. Tripathi, S.; Vaidya, S.; Ansari, K. U.; Ahmed, N.; Rivière, E.; Spillecke, L.; Koo, C.; Klingeler, R.; Mallah, T.; Rajaraman, G.; Shanmugam, M., Influence of a Counteranion on the Zero-Field Splitting of Tetrahedral Cobalt(II) Thiourea Complexes. *Inorg. Chem.* **2019,** *58*, 9085-9100.
104. Scholes, C. P.; Lapidot, A.; Mascarenhas, R.; Inubushi, T.; Isaacson, R. A.; Feher, G., Electron nuclear double resonance (ENDOR) from heme and histidine nitrogens in single crystals of aquometmyoglobin. *J. Am. Chem. Soc.* **1982,** *104*, 2724-2735.
105. Scholes, C. P.; Falkowski, K. M.; Chen, S.; Bank, J., Electron nuclear double resonance (ENDOR) of bis(imidazole) ligated low-spin ferric heme systems. *J. Am. Chem. Soc.* **1986,** *108*, 1660-1671.
106. Hoffman, B. M.; Venters, R. A.; Martinsen, J., General Theory of Polycrystalline ENDOR Patterns. Effects of Finite EPR and ENDOR Component Linewidths. *J. Magn. Reson.* **1985,** *62*, 537-542.
107. Hoffman, B. M.; Gurbiel, R. J., Polycrystalline ENDOR Patterns from Centers with Axial EPR Spectra. General Formulas and Simple Analytic Expressions for Deriving Geometric Information from Dipolar Couplings. *J. Magn. Reson.* **1989,** *82*, 309-317.

108. Holland, P. L.; Tolman, W. B., Three-Coordinate Cu(II) Complexes: Structural Models of Trigonal-Planar Type 1 Copper Protein Active Sites. *J. Am. Chem. Soc.* **1999,** *121*, 7270-7271.
109. Eckert, N. A.; Dinescu, A.; Cundari, T. R.; Holland, P. L., A T-Shaped Three-Coordinate Nickel(I) Carbonyl Complex and the Geometric Preferences of Three-Coordinate d^9 Complexes. *Inorg. Chem.* **2005,** *44*, 7702-7704.
110. Myers, W. K.; Scholes, C. P.; Tierney, D. L., Anisotropic Fermi Couplings Due to Large Unquenched Orbital Angular Momentum: Q-Band ^{1}H, ^{14}N, and ^{11}B ENDOR of Bis(trispyrazolylborate) Cobalt(II). *J. Am. Chem. Soc.* **2009,** *131*, 10421-10429.
111. Lloret, F.; Julve, M.; Cano, J.; Ruiz-García, R.; Pardo, E., Magnetic properties of six-coordinated high-spin cobalt(II) complexes: Theoretical background and its application. *Inorg. Chim. Acta* **2008,** *361*, 3432-3445.
112. Tierney, D. L., Jahn–Teller Dynamics in a Series of High-Symmetry Co(II) Chelates Determine Paramagnetic Relaxation Enhancements. *J. Phys. Chem. A* **2012,** *116*, 10959–10972.
113. Myers, W. K.; Duesler, E. N.; Tierney, D. L., Integrated paramagnetic resonance of high-spin Co(II) in axial symmetry: Chemical separation of dipolar and contact electron−nuclear couplings. *Inorg. Chem.* **2008,** *47*, 6701-6710.
114. Brown, T. G.; Hoffman, B. M., ^{14}N, ^{1}H, and metal ENDOR of single crystal Ag(II)(TPP) and Cu(II)(TPP). *Mol. Phys.* **1980,** *39*, 1073-1109.
115. For Ag(TPP), $\mathbf{P}(^{14}\mathrm{N})$ = [-0.692, +0.915, (-0.222)] MHz. Even in this single-crystal study, the third (smallest) nqc component was not directly measured in Cu,Ag(TPP), but was obtained from the requirement that $\sum_{i=1}^{3} P_i = 0$.
116. Kragskow, J. G. C.; Marbey, J.; Buch, C. D.; Nehrkorn, J.; Ozerov, M.; Piligkos, S.; Hill, S.; Chilton, N. F., Analysis of vibronic coupling in a 4f molecular magnet with FIRMS. *Nat. Commun.* **2022,** *13*, 825.
117. Brorson, M.; Schäffer, C. E., Orthonormal interelectronic repulsion operators in the parametrical d^q model. Application of the model to gaseous ions. *Inorg. Chem.* **1988,** *27*, 2522-2530.
118. Use of ζ = 425 cm^{-1} (~80% of free-ion value) gives $\mathbf{g'}$ = [5.93, 2.88, 1.76] and $2D^*$ = 71 cm^{-1}.
119. Atanasov, M.; Ganyushin, D.; Sivalingam, K.; Neese, F., A Modern First-Principles View on Ligand Field Theory Through the Eyes of Correlated Multireference Wavefunctions. In *Molecular Electronic Structures of Transition Metal Complexes II*, Mingos, D. M. P.; Day, P.; Dahl, J. P., Eds. Springer Berlin Heidelberg: Berlin, Heidelberg, 2012; pp 149-220.

120. Bendix, J.; Brorson, M.; Schäffer, C. E., Accurate empirical spin orbit coupling parameters ζ_{nd} for gaseous nd^q transition metal ions. The parametrical multiplet term model. *Inorg. Chem.* **1993,** *32*, 2838-2849.
121. Stoian, S. A.; Vela, J.; Smith, J. M.; Sadique, A. R.; Holland, P. L.; Münck, E.; Bominaar, E. L., Mössbauer and Computational Study of an N_2-Bridged Diiron Diketiminate Complex: Parallel Alignment of the Iron Spins by Direct Antiferromagnetic Exchange with Activated Dinitrogen. *J. Am. Chem. Soc.* **2006,** *128*, 10181-10192.
122. Sinnecker, S.; Slep, L. D.; Bill, E.; Neese, F., Performance of Nonrelativistic and Quasi-Relativistic Hybrid DFT for the Prediction of Electric and Magnetic Hyperfine Parameters in ^{57}Fe Mössbauer Spectra. *Inorg. Chem.* **2005,** *44*, 2245-2254.
123. Greer, S. M.; Gramigna, K. M.; Thomas, C. M.; Stoian, S. A.; Hill, S., Insights into Molecular Magnetism in Metal–Metal Bonded Systems as Revealed by a Spectroscopic and Computational Analysis of Diiron Complexes. *Inorg. Chem.* **2020,** *59*, 18141-18155.
124. Greer, S. M.; Üngor, Ö.; Beattie, R. J.; Kiplinger, J. L.; Scott, B. L.; Stein, B. W.; Goodwin, C. A. P., Low-spin 1,1′-diphosphametallocenates of chromium and iron. *Chem. Commun.* **2021,** *57*, 595-598.
125. Goodwin, C. A. P.; Giansiracusa, M. J.; Greer, S. M.; Nicholas, H. M.; Evans, P.; Vonci, M.; Hill, S.; Chilton, N. F.; Mills, D. P., Isolation and electronic structures of derivatized manganocene, ferrocene and cobaltocene anions. *Nature Chemistry* **2021,** *13*, 243-248.
126. Greer, S. M.; McKay, J.; Gramigna, K. M.; Thomas, C. M.; Stoian, S. A.; Hill, S., Probing Fe–V Bonding in a C_3-Symmetric Heterobimetallic Complex. *Inorg. Chem.* **2018,** *57*, 5870-5878.
127. Grant, C. V.; Ball, J. A.; Hamstra, B. J.; Pecoraro, V. L.; Britt, R. D., ^{51}V ESE-ENDOR Studies of Oxovanadium(IV) Complexes: Investigation of the Nuclear Quadrupole Interaction. *J. Phys. Chem. B* **1998,** *102*, 8145–8150.

For Table of Contents Only

Synopsis. High-spin (S > 1/2), low coordination number complexes are of interest as single molecule magnets (SMMs). The β-ketiminate (nacnac) ligand can support such complexes, here of general formula (nacnac)MX, where M = Fe^{II} (S = 2) and Co^{II} (S = 3/2), and X = Cl^- and CH_3^-. Advanced paramagnetic resonance spectroscopy reveals the zero-field splitting (zfs) in these complexes and theory explains the origin of zfs and the complexes' overall electronic structure.